



**The Role of The Coriolis Force on Deep Marine Gravity Currents
in Sinuous Channels**

being a thesis submitted in fulfilment of the
requirements for the degree of

Master of

Physical Geography

in the University of Hull

by

Nilufan, Xiaokaiti

July 2023

COPYRIGHT STATEMENT GOES HERE – [Get guidance](#)

Below this line is a hidden Section Break (Next Page). [DO NOT DELETE THIS!](#)

You can see hidden elements by using the Show/Hide option  on the home ribbon.

Acknowledgements

It feels exciting and emotional to finally be writing this, which means my time as a Master student at EEI must be drawing to an end. I have grown unimaginably both in academic and personal life. There are so many people that I would like to thank and whom I have been extremely lucky to have all along.

First and foremost, I would like to express my deep and sincere gratitude to my supervisors Robert M. Dorrell, Robert E. Thomas, Jeff Peakall and Daniel Parsons, thank you for giving me the utmost support throughout my time in Hull. Biggest thanks to Rob D, giving me this golden opportunity to have one of the most amazing experiences of my life. I couldn't finish my thesis without his endless support from academic writing to data analysis of my research. He was always here for me anytime to answer my questions relating to data processing and math. I have saved a lot of time by using the MatLab skills studied during my masters, and I'm confident that these skills will serve me well in my future career. Rob T is thanked for his endless patience and help during my times of frustration. Academically, he was willing to explain anything again and again without complaint until I fully understood it. Also, thanks for helping to frame my English in a much more formal and British way. In life, he was always generous with his encouragement, telling me that I was doing well, and teaching me how to balance life and work. Elena Bastianon is officially not in my supervisory team, but she was more than a supervisor to me. She was always there for all my questions, sometimes even it's not her field of study. She is also like a sister to me, she was not only concerned about my thesis, but also concerned about my health, my life and everything, which made me feel cared for.

Next, I would like to appreciate the administration teams in Energy and Environment Institute for their support that makes my time in Hull go very smoothly.

Also, I would like to thank everyone in Grenoble project to share the data and every detail of the experiments with me. I wouldn't have any results without this.

I would like to thank my friends in the UK, who worked, studied, travelled with me and helped me. A special thanks to Medina, who made my time in UK unexpectedly wonderful. Her support and company made me feel less alone.

I wouldn't be where I am today if it wasn't for my family. I am forever indebted to Mom and Dad, both for their unconditional support and love. Thank you for allowing me the total freedom to make my own choices and mistakes. Thanks to my one and only sister Niluza for her support and help. Especially taking her time out to take care of my son when I had to work on my thesis.

Thanks to my dearest son Zufar. I'm more than grateful that you came into my life and lit up my world when I had hit rock bottom. You are and you will always be my motivation to live.

Finally, biggest thanks to my soulmate, my best friend and my husband Zulpikar. This is probably the only one page of the paper he is interested in. Even though you showed a total indifference to my research, you did everything in your power to help me through every stage of my masters in the last four years. Thank you for coming to Hull to study with me and making me feel like home. Thank you for your unconditional support and the positive energy you've been giving me. Thank you for being there for me in every chapter of my life since high school. My heart is filled with gratitude.

Abstract

Gravity currents can be generated by density differences created by high suspended sediment concentrations in the form of turbidity currents, which can also transport significant volumes of near surface waters into the deep ocean. These flows are often concentrated in downslope channels that link and act as conduits from the continental shelves to the deep sea. Thus, understanding these mixing and exchange processes are critical to furthering our understanding of key ecosystems, the global carbon cycle and climate.

Many parameters affect density-driven flow dynamics, including density difference, bed roughness, and bottom slope. At large-scales, in real-world environments, the rotational motion of the earth generates pseudo-forces, i.e., Coriolis force that increase with latitude. In extreme limits this may become as important as the inertial force of average fluid motion. As such, this force also affects flow dynamics.

The formation and development of submarine channels are influenced by dynamic interaction of turbidity currents with the seafloor and the force acting on the flow. Laboratory experiments were conducted using world's largest rotating platform to investigate how the Earth's rotation might influence the internal flow structure and secondary flow at a bend apex. The downstream and cross stream velocity, as well as the density data for various rotating rates, across a range of Rossby numbers were gathered and analysed in order to investigate how buoyancy & velocity of channelized turbidity currents effect ambient fluid entrainment under different Rossby numbers (RO).

It is suggested that enhanced secondary flow with increasing Coriolis force results in reduced mixing. Coriolis force is responsible for changes in the direction of the bottom boundary layer of a gravity current and the location of the maximum velocity core, leading to result in uneven right and left-turning bends. The denser fluid, on the other hand, always remains close to the outer bend, creating a hydraulic mechanism for stabilizing bend evolution at higher latitudes. Strong Coriolis forces, in addition, can change the course of near-bed secondary flow.

Table of Contents

Acknowledgements.....	i
Abstract.....	iii
List of Figures	vi
List of Tables	x
List of Equations.....	xi
Chapter 1 Introduction	12
Chapter 2 Literature Review	14
2.1 Fundamental Controls on Gravity Currents	14
2.1.1 Reynolds Number: Turbulent Mixing	16
2.1.2 Froude and Richardson Numbers: Gravitational Forcing	17
2.1.3 Rossby Number: Rotating Frames of Reference	18
2.2 Turbidity Currents	20
2.2.1 Natural Occurrence of Turbidity Currents.....	21
2.2.2 Velocity and Density Profiles.....	23
2.2.3 Turbulent Mixing.....	26
2.3 Partially Confined Turbidity Currents.....	27
2.3.1 A note on Centrifugal Forces.....	29
2.3.2 A Note on Pressure Gradients.....	29
2.3.3 Flow Dynamics in Sinuous Channels	30
2.4 Latitudinal Control on Turbidity Currents	32
2.4.1 Ekman Layers	36
2.5 Summary	37
Chapter 3 Methodology.....	39
3.1 General description of the experiments	39
3.2 Experimental Parameters.....	40
3.3 Instrumentation and Data Acquisition	45
Chapter 4 Results.....	46
4.1 Density Profiles	46

4.2	Downstream Flow Velocity	51
4.3	Cross-Stream Flow Velocity.....	53
Chapter 5	Discussion.....	59
5.1	Time Average Flow Parameters	59
5.2	Coriolis Controls on Flow Dynamics	61
5.3	Experimental Anomalies	64
Chapter 6	Conclusions	66
6.1	Future work.....	67
References	70

List of Figures

Figure 1 : Coriolis effect diagram demonstrating how an item traveling in a north-south direction will appear to deviate to the right in the Northern Hemisphere and to the left in the Southern Hemisphere.....	19
Figure 2 : Schematic of a sediment gravity flow (Kneller & Buckee, 2000).....	21
Figure 3 : The two main mixing processes at the front of a gravity current: (a) Kelvin-Helmholtz billows; and (b) lobes and clefts (Simpson, 1986).....	22
Figure 4 : a) Collapse of downstream velocity data using characteristic height (from Kneller & Buckee (2000)) b) Characteristic velocity and c) density profiles for a saline gravity current (modified from Sequeiros et al (2010).	24
Figure 5 : Schematic diagram showing various characteristic density profiles (dashed lines) in density currents. a) Two-layer profile, b) Smooth profile, c) Stepped profile, d) Rouse-type profile. Figure from Kneller & Buckee (2000).	25
Figure 6 : Schematic view of 6 type of submarine channels at present-day sea levels. Figure from Peakall & Sumner (2015).....	28
Figure 7 : Schematic illustration of the centrifugal force arising from the rotation of the Earth. Showing gravity always pointing towards the centre of Earth, and the centrifugal force is perpendicular to the axis of the Earth. Note this is distinct from the centrifugal force that can arise from the choice of coordinate system in specific frame of reference, e.g., relative to a sinuous channel traversed by a flow.	29
Figure 8 : Illustration of the primary and secondary flow environments around a meander bend (Smit & Kaeser, 2016).	31
Figure 9 : The downstream velocity profiles (u) along the centreline at left. Cross-stream velocity field at the bend apex, with the contoured colours representing the v component at right. Panels a), b), c) and d) show the Coriolis parameters $f = 0 \text{ rad s}^{-1}$, $f = +0.25 \text{ rad s}^{-1}$, $f = -0.25 \text{ rad s}^{-1}$, and $f = -0.5 \text{ rad s}^{-1}$. Figure from Cossu & Wells (2010).	35
Figure 10 : (a) An illustration of the experiment channel at the Coriolis facility at LEGI in Grenoble. Position X1 and Position X2 along the channel were the palaces where data was collected. (b) A picture of the channel with a $R = 1.5$ radius of curvature, 11m long inside the rotating table, looking upstream. (c) The locations of the velocity measurement at two positions of X1 and X2 in the channel. (d) The precise location of the ADVs and the MSCTI conductivity probe that were employed in the studies (from Davarpanah Jazi et al (2020)).	39

Figure 11 : Vertical profiles of time-averaged gravity current buoyancy, defined as dimensionless excess density, at the second apex of the channel under different rotation rates ($Ro = \pm 8, \pm 4, \pm 2, \pm 1, \infty$) at 5 minute increments between 5 and 35 minutes. a) Flow in a non-rotational frame of reference, where the Rossby number ($RO = ULf$) equals infinity; b), d), f) and h) Flow in a rotating frame of reference, subject to increasing pseudo Coriolis force towards the outer bank at Rossby numbers, b) $Ro = +8$; d) $Ro = +4$; f) $Ro = +2$ h) $Ro = +1$; c), e), g) and i) Flow in a rotating frame of reference, subject to increasing pseudo Coriolis force towards the inner bank at Rossby numbers, c) $Ro = -8$; e) $Ro = -4$; g) $Ro = -2$, and i) $Ro = -1$47

Figure 12 : Contour maps of gravity current buoyancy, defined as dimensionless excess density, at the second apex of the channel under different rotation rates ($Ro = \pm 8, \pm 4, \pm 2, \pm 1, \infty$). a) Flow in a non-rotational frame of reference, where the Rossby number ($RO = ULf$) equals infinity. b), d), f) and h) Flow in a rotating frame of reference, subject to increasing pseudo Coriolis force towards the outer bank at Rossby numbers, b) $Ro = +8$, d) $Ro = +4$, f) $Ro = +2$, and h) $Ro = +1$. c), e), g) and i) Flow in a rotating frame of reference, subject to increasing pseudo Coriolis force towards the inner bank at Rossby numbers, c) $Ro = -8$; e) $Ro = -4$; g) $Ro = -2$, and i) $Ro = -1$49

Figure 13 : Normalised downstream velocity profile (U/U_{max}) of the flow at centreline of second apex under different rotation rates ($Ro = \pm 8, \pm 4, \pm 2, \pm 1, \infty$). a) Flow in a non-rotational frame of reference and in a rotating frame of reference, subject to increasing pseudo Coriolis force towards the outer bank (same direction as centrifugal force) at Rossby number ($RO = ULf$) equals infinity, +8, +4, +2, and +1. b) Flow in a non-rotational frame of reference and in a rotating frame of reference, subject to increasing pseudo Coriolis force towards the inner bank (opposite direction of centrifugal force) at Rossby number ($RO = ULf$) equals infinity, -8, -4, -2, and -1.51

Figure 14 : Contour maps of gravity current downstream velocity at the second apex of the channel under different rotation rates ($Ro = \pm 8, \pm 4, \pm 2, \pm 1, \infty$). a) Flow in a non-rotational frame of reference, where the Rossby number ($RO = ULf$) equals infinity. b), d), f) and h) Flow in a rotating frame of reference, subject to increasing pseudo Coriolis force towards the outer bank at Rossby numbers, b) $Ro = +8$, d) $Ro = +4$, f) $Ro = +2$, and h) $Ro = +1$. c), e), g) and i) Flow in a rotating frame of reference, subject to increasing pseudo Coriolis force towards the inner bank at Rossby numbers, c) $Ro = -8$; e) $Ro = -4$; g) $Ro = -2$, and i) $Ro = -1$. The zero-velocity line (black line) and maximum velocity line (white line) are added to the contour maps.52

Figure 15 : Cross-stream velocity profile of the flow at three different locations (10cm away from each wall and the centre of channel) of second apex under different rotation rates ($Ro = \pm 8, \pm 4, \pm 2, \pm 1, \infty$). Flow at clockwise rotating frame of reference, subject to increasing pseudo Coriolis force towards the outer bank (same direction as centrifugal force) at Rossby number ($RO = ULf$) equals infinity, +8, +4, +2, and +1 at a) 10cm away from left wall, b) at the centreline (channel width is 600mm), c) 10cm away from right wall. Flow at anticlockwise rotating frame of reference, subject to increasing pseudo Coriolis force towards the inner bank (opposite direction of centrifugal force) at Rossby number ($RO = ULf$) equals infinity, -8, -4, -2, and -1 at a) 10cm away from left wall, b) at the centreline (channel width is 600mm), c) 10cm away from right wall.54

Figure 16 : Cross-stream velocity profile of the flow at three different locations (10cm away from each wall and the centre of channel) of second apex under different rotation rates ($Ro = \pm 8, \pm 4, \pm 2, \pm 1, \infty$) with standard deviation error bars which represents the variation of the data. a) Flow in a non-rotational frame of reference, where the Rossby number ($R_O = U/Lf$) equals infinity. b), c), d) and e) Flow in a rotating frame of reference, subject to increasing pseudo Coriolis force towards the outer bank at Rossby numbers, b) $Ro = +8$, c) $Ro = +4$, d) $Ro = +2$, and e) $Ro = +1$. f), g), h) and i) Flow in a rotating frame of reference, subject to increasing pseudo Coriolis force towards the inner bank at Rossby numbers, f) $Ro = -8$; g) $Ro = -4$; h) $Ro = -2$, and i) $Ro = -1$55

Figure 17 : Contour maps of gravity current cross-stream velocity at the second apex of the channel under different rotation rates ($Ro = \pm 8, \pm 4, \pm 2, \pm 1, \infty$). a) Flow in a non-rotational frame of reference, where the Rossby number ($R_O = U/Lf$) equals infinity. b), d), f) and h) Flow in a rotating frame of reference, subject to increasing pseudo Coriolis force towards the outer bank at Rossby numbers, b) $Ro = +8$, d) $Ro = +4$, f) $Ro = +2$, and h) $Ro = +1$. c), e), g) and i) Flow in a rotating frame of reference, subject to increasing pseudo Coriolis force towards the inner bank at Rossby numbers, c) $Ro = -8$; e) $Ro = -4$; g) $Ro = -2$, and i) $Ro = -1$. The zero-velocity line (black line) and maximum velocity line (white line) are added to the contour maps.57

Figure 18 : Downstream velocity, density and gradient Richardson number (Equation 6) profiles of gravity current at the second apex of the channel under different rotation rates ($Ro = \infty, \pm 8, \pm 4, \pm 2, \pm 1, =$). a) Flow in a non-rotational frame of reference, where the Rossby number ($Ro = U/Lf$) equals infinity. b), d), f) and h) Flow in a rotating frame of reference, subject to increasing pseudo Coriolis force towards the outer bank at Rossby numbers, b) $Ro = +8$, d) $Ro = +4$, f) $Ro = +2$, and h) $Ro = +1$. c), e), g) and i) Flow in a rotating

frame of reference, subject to increasing pseudo Coriolis force towards the inner bank at Rossby numbers, c) $Ro=-8$; e) $Ro=-4$, g) $Ro=-2$, and i) $Ro=-1$. The critical $Rig=0.25$ is denoted by a red line.62

List of Tables

Table 1 : Range of fixed and variable flow parameters for the experiments.....	41
Table 2 : Experimental flow conditions.....	42

List of Equations

Equation

$$\frac{\partial \rho}{\partial t} + \nabla \cdot (\rho \mathbf{u}) = 0 \quad (1)$$

$$\frac{\partial \rho}{\partial t} + \nabla \cdot (\rho \mathbf{u}) = 0$$

Equation (2) $\nabla \cdot \mathbf{u} = 0$

Equation (3) $\frac{D\mathbf{u}}{Dt} = \frac{1}{\rho} \nabla \cdot \boldsymbol{\sigma} + \mathbf{F}$

Equation (4) $Re = \frac{\rho u L}{\mu} = \frac{u L}{\nu}$

Equation (5) $Fr = \frac{u}{\sqrt{g_0 L}} \equiv \frac{1}{\sqrt{Ri}}$

Equation (6) $Rig = -\frac{g}{\rho} \frac{\partial \rho / \partial z}{(\partial u / \partial z)^2}$

Equation (7) $Ro = \frac{U}{Lf}$

Equation (8) $P_{\text{shear}} = -\overline{u'_i u'_j} \frac{du_i}{dx_j}$

Equation (9) $P_{\text{buoy}} = -\frac{g}{\rho_a} \overline{\rho' w'}$

Equation (10) $h = \frac{(\int_0^\infty u dz)^2}{\int_0^\infty u^2 dz}$

Equation (11) $B|_{z=h} = 0$

Equation (12) $u|_{z=h} = 0$

Equation (13) $\left. \frac{dv}{dz} \right|_{z=h} = 0$

Chapter 1 Introduction

Gravity currents are driven by a density difference with the surrounding ambient fluid and are a ubiquitous phenomenon in environmental fluid dynamics (Middleton, 1993; Simpson & Britter, 1979; Simpson, 1982). Gravity currents such as dense overflows, sediment-laden turbidity currents and contourite flows, occur across large ranges of space and time scales (Simpson, 1999). In the oceans, turbidity currents, gravity currents driven by suspended sediment, are important mechanisms that transport material, and sediment, across large horizontal distances and contribute to cross-shelf mixing (Azpiroz-Zabala et al, 2017). As the currents travel downslope in the continental shelf, they accelerate and interact with the bed entraining sediment, and entraining fluid from the ambient water above (Meiburg & Kneller, 2010). Submarine canyons and channels are among the most significant and substantial sedimentary features on the ocean floor, serving as a key pathway for the interchange of materials between the shelf and the deep ocean. Turbidity currents can result from geological disturbance events like earthquakes or collapsing slopes (Meiburg & Kneller, 2010). The turbid water rushes downward after turbidity is set in action, which can change the physical structure of the seafloor by eroding vast areas and forming underwater canyons (Parsons et al, 2007). Here the dynamics of turbidity currents, and their role in development of seafloor channels, are the focus of this study.

Flows at large scales, such as atmospheric winds and oceans currents, can be deflected by the Earth's rotation (generating pseudo Coriolis forces). Coriolis forces are a fictitious force that describes the apparent deviation and curvature of a flow, from a stationary frame of reference, as the Earth rotates underneath it (Arnol'd, 2013). These forces increase with latitude and deflect flow to right in the Northern Hemisphere and to the left in the Southern Hemisphere for a north-south flow. It has been observed that submarine channels and canyons are also affected by the effect of Coriolis forces (Akhmetzhanov et al, 2007; Hesse et al, 1987) which is discussed later in the thesis. Especially, buoyancy and velocity effects ambient entrainment are the key focus of this study. Turbidity currents that flow within oceans are large enough to be impacted by the rotation of the Earth, and the Coriolis forces can drive secondary circulations and decide where erosion and deposition occurs (Akhmetzhanov et al, 2007; Hesse et al, 1987). This is especially important for the formation of submarine channels located at mid-high latitudes and those with large bends which flow dynamics are dominated by Coriolis forces, and turbidity

currents under Coriolis forces can also affect levee asymmetry and channel sinuosity (Peakall et al, 2012).

In conclusion, the dynamic interplay between turbidity currents and the seafloor, as well as the forces acting on the flow control submarine channel development. (De Leeuw, 2016). The aim of this project is to investigate the influence of Coriolis forces on the internal flow structure and secondary flow at a bend apex, and thus to link turbidity current flow dynamics to development of seafloor channels. In particular, a key control on the transport of sediment by turbidity currents is the mixing between flow and ambient fluid, which plays an essential role in controlling run out distances and sediment deposition (Hacker et al, 1996). The ambient entrainment is strongly impacted by velocity (downstream and cross-stream) and buoyancy of the flow, and these two factors can vary under different Rossby numbers. Previous work has not considered how Coriolis forces may impact mixing and ambient fluid entrainment.

To achieve these aims, the effects of Coriolis force on the mixing efficiency of submarine gravity currents in a sinuous channel is here systematically analyzed based on novel experimental data. In this study the downslope and cross slope velocity and the density of a submarine turbidity current is analyzed for different rotating rate, at laboratory scale. [The experimental system has some similarities to idealised cross-shelf contour current systems.](#)

Chapter 2 reviews the literature describing gravity current forms, dynamics and the controls, especially the formation and dynamics of turbidity currents. The literature review focuses on turbidity currents in sinuous channels and also mixing between the current and ambient flow. Chapter 3 outlines the methodology adopted in this thesis, introducing the experiment in detail with how the data were captured and analysed. Chapter 4 presents and describes the results of the study. Density and velocity (downstream and cross-stream) profiles and velocity contour maps are presented. Chapter 5 discusses those results, placing them into wider context within the literature and satisfying the aims and answering the objectives of the thesis. Chapter 6 presents the conclusions of the thesis and provides suggestions for future work.

Chapter 2 Literature Review

Gravity currents are driven by density difference such as salinity, sediment, temperature; by interacting with the ambient water they can mix and change their characteristics (Maslin et al, 2006; Piper & Deptuck, 1997). However, additional forces may enhance mixing between turbidity currents and the ambient fluid. For example, the Coriolis force, which is due to Earth's rotation and the centrifugal force, arising at a channel bend, strongly influences turbidity current mixing (Dorrell et al, 2013; Kelly et al, 2019). Because of the interaction between turbidity currents and pseudo forces, the force required for Newton's laws of motion to be valid in a non-inertial frame of reference, despite it being physically evident but non-existent (American Heritage® Dictionary of the English Language, 2023), the flow can overspill from the channel levee and create turbidite deposits. This process is particularly important and significantly regulates the amount and the grain of sediment that overspills, determining the shape of the channel levee.

2.1 Fundamental Controls on Gravity Currents

In this section the key concepts controlling gravity current dynamics are introduced, by considering the fundamental equations and non-dimensional parameters for the motion of fluid. In particular, since the scale of gravity currents that we intend to study are strongly impacted by the effect of Earth's rotation, the rotating frame of reference with pseudo-forces (Coriolis force and centrifugal forces) are highlighted. A consequence of Earth's rotation is the development of key flow features; for example, near boundaries an Ekman layer develops (Davaranah Jazi et al, 2020), where Coriolis forces are in balance with frictional force, and forcing on secondary flow, modifying the balance of centrifugal forces and hydrostatic pressure gradients.

The motion of incompressible, Newtonian fluid is governed by the three-dimensional mass- and momentum-conservation equations (Acheson, 1990). As mass cannot be generated or destroyed, inflows, outflows, and changes in the storage of mass within a system must all be in balance. The law of mass conservation can be formulated mathematically and it is expressed as the continuity equation (Pedlosky, 1987):

$$\frac{\partial \rho}{\partial t} + \nabla \cdot (\rho u) = 0 \quad (1)$$

Where ∂ is the partial derivative operator, ρ is the density, t is the time, ∇ is the divergence, and \mathbf{u} is the flow velocity vector field. Equation

$$\frac{\partial \rho}{\partial t} + \nabla \cdot (\rho \mathbf{u}) = 0 \quad (1)$$

can be simplified by assuming that changes in density in space and time are negligible except when multiplied by g , the acceleration due to gravity. Applying this simplification to equation

$$\frac{\partial \rho}{\partial t} + \nabla \cdot (\rho \mathbf{u}) = 0 \quad (1)$$

yields the Boussinesq approximation (Boussinesq, 1897; Tritton, 2012):

$$\nabla \cdot \mathbf{u} = 0 \quad (2)$$

Momentum conservation states that the momentum of an isolated system is constant if there are no external forces acting on that system (Batchelor, 1967). Written in non-conservative form:

$$\frac{D\mathbf{u}}{Dt} = \frac{1}{\rho} \nabla \cdot \boldsymbol{\sigma} + \mathbf{F} \quad (3)$$

where D/Dt is the total or material derivative, $\boldsymbol{\sigma}$ is the stress tensor – the second order tensor consists of completely specified nine components which are defined by the direction stress acts and the orientation of the surface upon which it is acting, and \mathbf{F} are the forces acting on the body of fluid (for example viscous dissipation, gravitational forces or Coriolis force).

Without loss of generality Equations (1) – (3) can be rewritten using characteristic dimensional scales, typically a flow velocity scale and a length scale. Appropriate normalisation of the governing equations results in the generation of non-dimensional parameters. Such non-dimensional parameters are extremely useful, as:

- I) a priori of any analysis non-dimensional parameters can be used to understand primary controls on the dynamics of the fluid flow, here turbidity currents;
- II) non-dimensional parameters enable scaling and comparison of different flows in different context and settings, for example comparing physical and numerical models with real world processes (Paola et al, 2009).

The density differential, frictional drag, and bottom slope are only a few of the variables that determine density-driven flow dynamics (Cenedese et al, 2004). For large-scale flows, the rotation of the planet produces a non-negligible Coriolis force that increases with latitude

(Cossu & Wells, 2010). This force consequently has an impact on flow dynamics. Here three key non-dimensional parameters, which are known to control the dynamics of gravity currents at large scale in rotating reference frames, are introduced below.

2.1.1 Reynolds Number: Turbulent Mixing

For turbidity currents, mixing by fluid turbulence is a key control on flow dynamics. It determines the suspension of particulate material, providing the motive force for the flow. Mixing is also responsible for the entrainment of fresh water, from the ambient (Cenedese et al, 2004). Turbulence is characterised by the Reynolds number (Re) as the dimensionless ratio of inertial and viscous forces (parameterised within F, Equation (3)):

$$\text{Re} = \frac{\rho u L}{\mu} = \frac{u L}{\nu} \quad (4)$$

Here u is the characteristic velocity of the fluid, L is a characteristic linear dimension (for example the flow depth), μ is the dynamic viscosity of the fluid, ν is the kinematic viscosity of the fluid. The Reynolds number can be used to define flow regimes (Munson et al, 2013), determining the relative importance of turbulence and laminar flow (Reynolds, 1883).

- For low Reynolds numbers ($\text{Re} < 2000$), fluid behaviour is dominated by viscous forces, and the flow is predominantly laminar.
- For intermediate Reynolds numbers ($2000 \leq \text{Re} < 4000$), the flow is transitional, with characteristics that are partly laminar and partly turbulent.
- For high Reynolds numbers ($\text{Re} \geq 4000$), fluid behaviour is dominated by inertial forces, and the flow is turbulent.

In real-world turbidity currents, flow velocity ~ 10 m/s, depth ~ 100 m and viscosity $\sim 10^{-6}$ m² s⁻¹ (Peakall & Sumner, 2015). Reynold numbers are therefore $\text{Re} \sim 10^9$, implying the flow is highly turbulent. Physical experiments and numerical studies are constrained by scale and computational resource; therefore, it is often assumed that as long as flows are turbulent $\text{Re} \gg 2000$ there is a similarity between modelled and real-world dynamics (Peltier & Caulfield, 2003). However, a critique of previous work (Cenedese & Adduce, 2008; Cenedese et al, 2004;

Cossu & Wells, 2013; Cossu et al, 2010) is that small scale laboratory experiments are not large enough to approximate the turbulent dynamics of real-world flows.

2.1.2 Froude and Richardson Numbers: Gravitational Forcing

The difference in density from the ambient flow drives gravity currents. The ratio between inertia and gravity forces, defined as the Froude number (Fr) is thus a crucial factor in controlling an unstratified flow dynamics; Froude number modelling relaxes the requirement on Re, and as such neglects viscous effects and is only applicable to fully turbulent flows. For gravity currents, densimetric Froude number is commonly used (as the action of gravity is dependent on the fractional density difference between current and ambient). The inverse Froude number squared is also referred to as the Richardson number (Ri) (Munson et al, 2013; White, 1999).

$$Fr = \frac{\bar{U}}{\sqrt{g'L}} \equiv \frac{1}{\sqrt{Ri}} \quad (5)$$

Here \bar{U} is depth-averaged current velocity, the length scale L is the hydraulic depth (Baines, 1998) and g' is the reduced gravity. The reduced gravity ($g' = g(\rho_2 - \rho_1)/\rho_1$) is defined as in terms of the difference between density of the current (ρ_2), and the density of the ambient (ρ_1) (Kneller & Buckee, 2000). In general, based upon the Froude number (Fr), the flow can be classified as follows (White, 1999):

- When $Fr < 1$, flow is sub-critical; the wave velocity is greater than the flow velocity, causing a wave created by an obstruction to propagate upstream.
- When $Fr = 1$, the flow is critical; its speed is nearly equal to that of the surface waves.
- When $Fr > 1$, the flow is super-critical, and it is impossible for waves to move upstream.

According to Ashford (1985), gradient Richardson number, or Rig , expresses the ratio of buoyancy to flow shear, gives an estimate of the stability of the flow, which in this context relates to how effectively the turbulence can be damped by the flow:

$$Rig = -\frac{g}{\rho} \frac{\partial \rho / \partial z}{(\partial u / \partial z)^2} \quad (6)$$

$Ri < 1/4$ is a requisite for velocity shear to overcome the stratified fluid's tendency to remain stratified, and certain turbulence generally occurs. When Ri is large, turbulent mixing is usually inhibited due to the difficulty of mixing due to buoyancy (Turner, 1979).

Given the dearth of coupled observational data of turbidity current density and velocity, there is a lack of knowledge of how Rig varies within real-world turbidity currents (Dorrell et al, 2016). This is important as Rig characterise stability and thus mixing process within turbidity currents, their capacity to suspend particulate material, distribute it within the flow and entrain ambient fluid.

2.1.3 Rossby Number: Rotating Frames of Reference

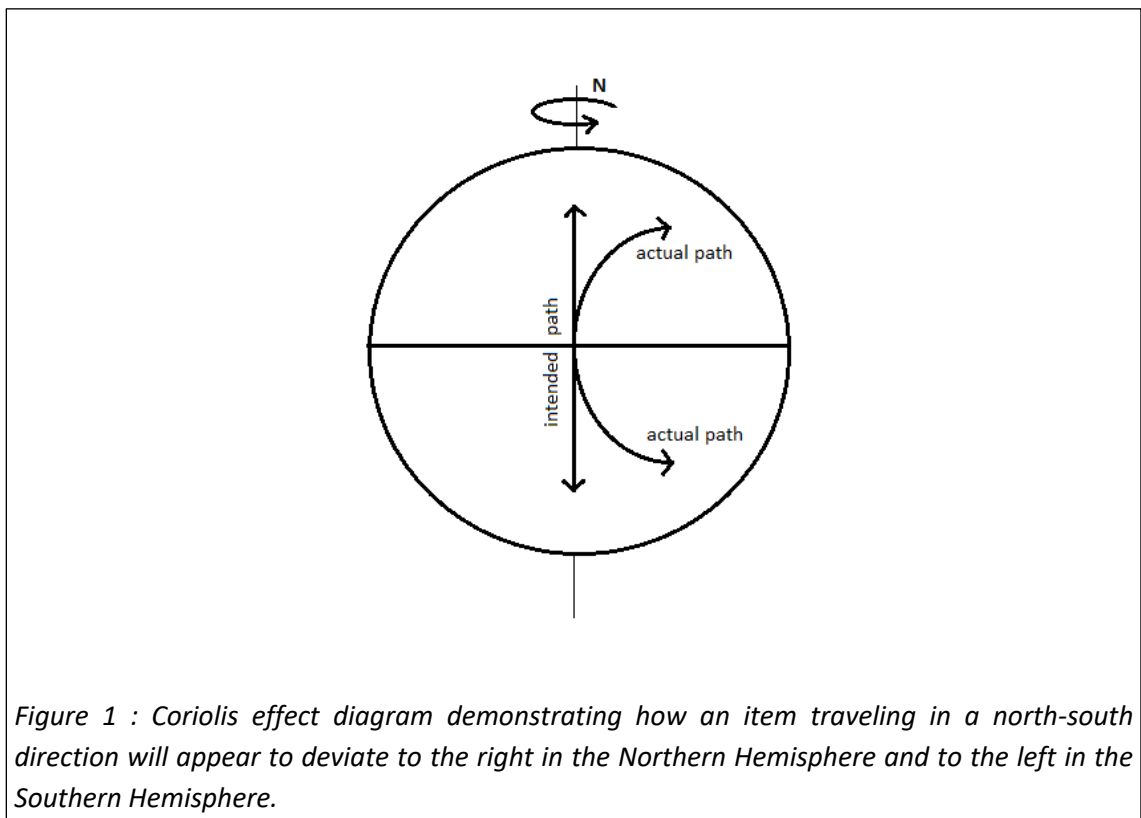
A rotating frame of reference is a reference system for non-uniform linear motion relative to an inertial reference frame (Arnol'd, 2013). The Earth's surface is a common example in geophysical fluid dynamics (Vallis, 2016). Pseudo-forces (also called fictitious forces) operate on all fluids whose motion can be explained using a rotating frame of reference (Bhatia, 1997). Example of pseudo-forces on Earth are i) the Centrifugal force, which is the apparent force that makes an object move outwardly away from the centre when it is moving around a curve; ii) the Coriolis force, which is also an apparent force that deflects a moving object due to the Earth's rotation (Arnol'd, 2013). These two forces are responsible for the secondary circulation in a sinuous channel, where they determine location of erosion and deposition.

The Coriolis force is an inertial force acting on an object moving within a rotating frame of reference (Persson, 1998). The Coriolis force causes an apparent deflection of an object's path in relation to the rotating frame of reference, to the right in Northern Hemisphere, and to the left in Southern Hemisphere (Figure 1). The motion of the coordinate system gives the impression that the item is deviating from its path, although it is not.

The Rossby number (R_0) is the ratio of inertial force to Coriolis force and compares the velocity and length scales of motion to the rotation rate of the Earth (Banerjee, 2004; Price, 1994):

$$R_0 = \frac{U}{Lf} \quad (7)$$

where U and L are respectively characteristic velocity and length scales of the phenomenon. The Coriolis frequency (f) is computed as $f=2\Omega\sin\varphi$, where Ω is the angular frequency of a planetary rotation and φ the latitude. R_0 is frequently used in geophysical phenomena in the oceans and atmosphere, where it portrays the importance of Coriolis acceleration caused by planetary rotation (Boubnov & Golitsyn, 1995). A large Rossby number indicates the effect of Coriolis force



is not significant. In contrary, smaller Rossby number indicates the role of rotation is significant

(Barry, 2009). The sign of the Rossby number tells if the object is rotating clockwise as it imitates the northern hemisphere, and anticlockwise as in the southern hemisphere.

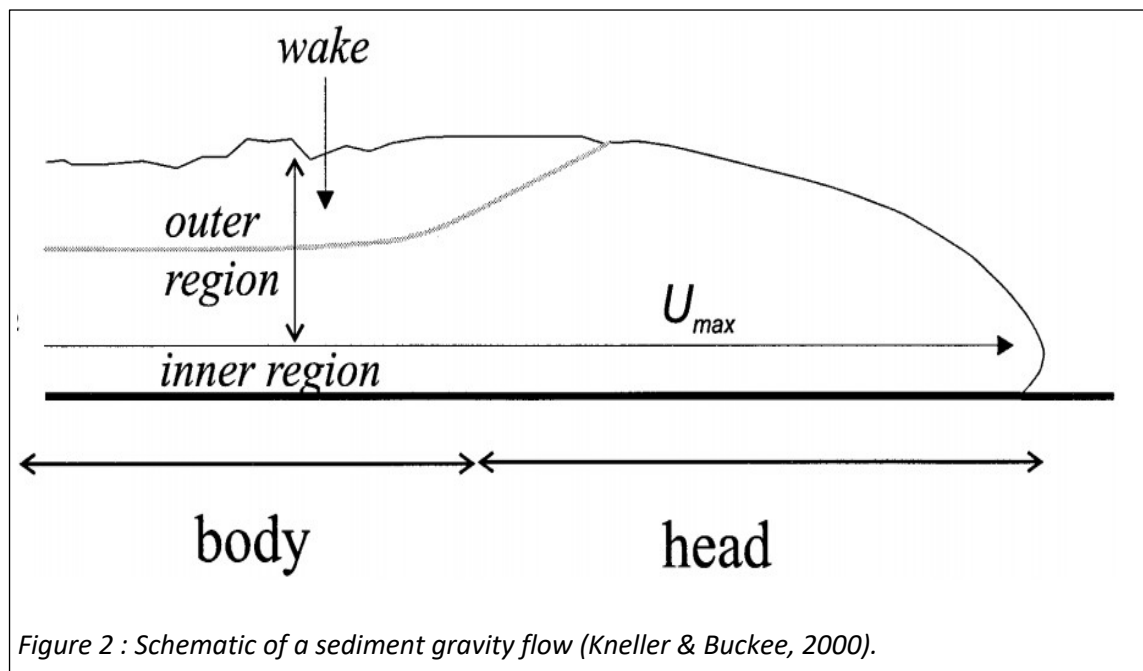
2.2 Turbidity Currents

Gravity currents, flows driven by the action of gravity on the density difference between flow and ambient fluid, play an essential role in the transport of fluid, sediment, nutrients and pollutants from the relatively shallow waters of the continental shelf to the abyssal plains of the deep ocean (Nittrouer & Wright, 1994). Density currents often drain through seafloor channels (Simpson, 1999). Examples of oceanic density currents are dense current flows from marginal seas, e.g. the Celtic Sea, North Atlantic Ocean initiated by strong cooling at the surface (Ivanov et al, 2004) or massive overflows originating in semi-enclosed basins such as Nordic seas (Legg et al, 2009). Submarine channels are extensive geological features, traversing thousands of kilometres of seafloor, that are formed by the passage of successive turbidity currents over thousands of years, and that are still evolving due to the process of entraining and deposition by turbidity currents (Maslin et al, 2006; Piper & Deptuck, 1997). Since gravity currents are vital to the transfer of water and sediment between the continental shelf and the deep sea, exploring their dynamics is critical to enhance understanding of those exchanges, entrainment and, further, overall oceanic circulation.

2.2.1 Natural Occurrence of Turbidity Currents

Whether in a natural situation or a man-made one, density driven flows, gravity currents or buoyancy currents can exist. Turbidity currents coming down from the continental shelf periodically disturb the seafloor (Hage et al, 2018). The presence of sand and silt in abyssal plains is proven to be due to the sediment being transported by turbidity currents. (Meiburg & Kneller, 2010; Simpson, 1982). The evolution of seafloor topography is controlled by the turbidity currents via deposition and erosion (Meiburg & Kneller, 2010; Talling et al, 2015). Such gravity currents flow from the continental shelves to the deep ocean (Meiburg & Kneller, 2010). The flows themselves display distinctively well-defined 'body and head' (and tail) areas with the head being thicker than the body (Figure 2), and the body forms the majority of the flow.

Although the body, head tail depicts a picture of a two-dimensional flow, gravity currents can be strongly three dimensional. It is well established that three-dimensional behaviour at the head is related to two forms of instability (Figure 3) which are responsible for mixing: (1) Kelvin-



Helmholtz billows, which gather above the front of the dense flow in the zone of velocity shear, and (2) lobes and clefts, which are created by the impact of the ground on the bottom half of the head. The dominant instabilities are Kelvin-Helmholtz billows, which are generated by the opposite motion of contacting layers moving at differing densities and velocities, breaking behind the head and causing entrainment of ambient fluid (Nogueira, 2014). The distortion,

even breaking up, of the Kelvin-Helmholtz billows is usually due to the subordinate convective instability called lobes and clefts that are created by the mixing of the less dense flow under the 'nose', i.e. the leading edge of the flow (Simpson, 1986). Because of the intense mixing that results in high levels of entrainment, the head may be as much as twice as thick as the body that comes behind it (Simpson, 1986).

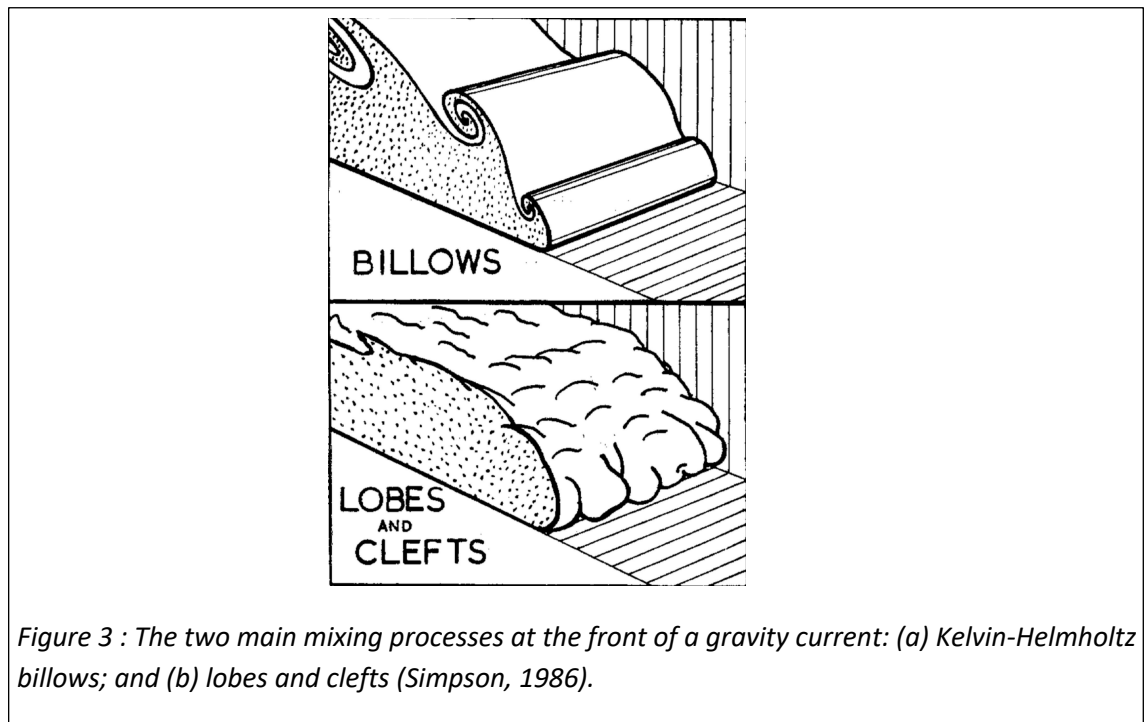


Figure 3 : The two main mixing processes at the front of a gravity current: (a) Kelvin-Helmholtz billows; and (b) lobes and clefts (Simpson, 1986).

Even though the body often constitutes the majority of the flows, little is known about its structure (Wells & Dorrell, 2021). For example, Dorrell et al (2019) hypothesized that the body of the gravity current may evolve to resemble a zonal jet in structure, as driven by mass and momentum redistribution by flow-scale internal waves that propagate in a density stratified medium. Due to internal velocity variation, these waves may help the flow develop a critical layer by preventing mixing and the dilution of the lower part of the current; this changes the expected structure of the density and velocity profiles. Internal gravity waves suggest that the body may not be statistically stable as is typically assumed. Since internal waves have the capacity to transmit horizontal momentum inside a flow and deposit it at crucial layers, they may be required to explain long duration gravity current dynamics. (Marshall et al, 2021b). Further, Marshall et al (2021a) demonstrated that increasing the ratio of turbulent momentum to mass diffusion, i.e. the turbulent Schmidt number from 1, results in significant structural changes in gravity current body that are not visible with increasing the Reynolds number in the range under consideration.

The considerable mixing at the Interface between two fluids plays a significant part in flow dynamics (Simpson, 1999). This action is crucial for sedimentologists to consider since it has the potential to significantly affect erosion and sediment transport by the current (Middleton, 1993; Straub et al, 2008).

Gravity currents have large amounts of turbulent mixing at the head region, in comparison the mixing process in the body region may be of reduced intensity (Simpson, 1999). The thickness of the head remains quasi-steady for currents moving on horizontal surfaces but the relative size of the head increases with slope angle for those flowing downslope (Simpson, 1999). Because pressure rather than gravitational forces dominates slopes steeper than 3° , the front velocity is only slightly dependent on slope, which causes the thickness of the head to rise (Middleton, 1966b).

Despite the importance of the head the duration of turbidity currents can be very long, order days to weeks (Azpiroz-Zabala et al, 2017). Dynamics within the body of the flow are therefore crucial to explaining the transport of material by turbidity currents. Velocity and density profiles of the flow determine how much, and what, material is transported and how quickly. Further, velocity and density profiles control turbulent suspension. Turbulent suspension of material provides the motive force to drive flows, keeping material in suspension: a process referred to as auto-suspension (Parker et al, 1986). In particular, turbulent mixing dictates the ambient fluid's entrainment. The entrainment of ambient fluid balances the dissipation of the turbulent kinetic energy, by raising the centre of suspended mass. Dissipation of energy ultimately slows the flow down, resulting in deposition. The extant paradigm is that entrainment of ambient fluid, and thus dissipation of energy, scales with Froude number squared. However, this dissipation is too large to enable prediction of turbidity current run out – despite observations that flows travel for thousands of kilometres of shallows slopes: this is the auto-suspension paradox (Parker et al, 1986; Wells & Dorrell, 2021).

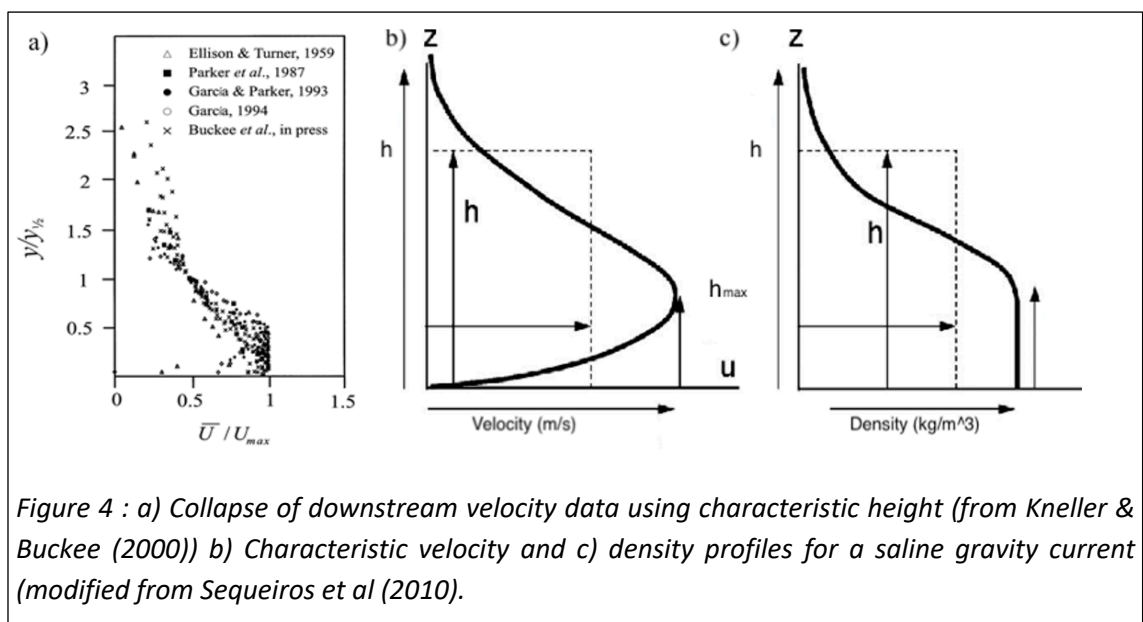
2.2.2 Velocity and Density Profiles

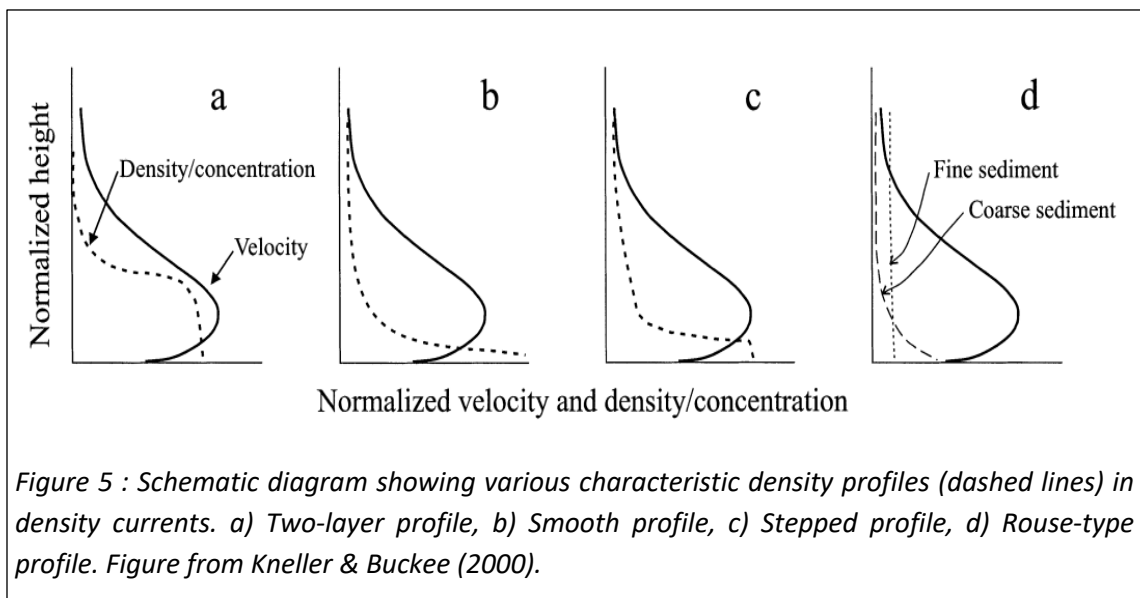
In contrast to the head of a gravity current, the body has a different mass-momentum balance (Middleton, 1993). The body of a gravity current is relatively stable and uniform in thickness compared to the head. Because the amount of dense fluid on the back of the head that is mixed with the ambient is lost into the ambient and loses its forward momentum, turbulent mixing at

the back of the head has no effect on the body's dynamics (Lowe et al, 2002). The vertical structure of a gravity current is important for understanding further processes and dynamics involved. Density, velocity and turbulence profiles dictate how turbidity currents travel for thousands of kilometres along the seafloor and are essential to understand the mixing process (Klaucke et al, 1998).

Gravity flows are characterised mainly by their velocity and density profile characteristics (Ellison & Turner, 1959; Stacey & Bowen, 1988). The typical vertical velocity and density profile of a gravity current is shown in Figure 4. The velocity maximum is close to the bottom of the current and divides the flow to an inner region, which has a positive velocity gradient, and an outer region with negative velocity gradient (Meiburg & Kneller, 2010; Tesaker, 1969). The thickness of the inner region is often reported to be less than half of the outer region. The ratio of upper and lower boundary shear and drag forces decides the height of the velocity maximum (Kneller et al, 1997; Middleton, 1966a) and height of the velocity maximum is about 0.2-0.3 of the current height in many experiments (Kneller et al, 1997).

Sequeiros et al (2010) observed that independent of the bed type, the subcritical flows, $Fr < 1$, show vertical position of the velocity maximum is slanted toward the interface between the flow and ambient. Conversely, when bed forms are absent, the vertical position of the velocity maximum is biased toward the bed to an extent that varies with bed type in supercritical flows (Sequeiros et al, 2010). This was argued to entrainment in supercritical flows acting to mix the upper layer of the flow and lower the velocity maximum. (The Froude number is viewed as an estimate of the Richardson gradient number, Equation (6), across the flow – ambient fluid





interface, and thus the stability of the flow). These conclusions were disputed by Stagnaro & Bolla Pittaluga (2014) who argued, albeit from a limited data set, that the densimetric Froude number of the current has no effect on velocity profiles. The experiments of Sequeiros et al (2010) exhibited slight stratification in subcritical flows and continuous stratification in supercritical flows. However, flows in the middle and lower parts of submarine channels exhibit stratification, and the middle and upper part of submarine channels are characterised by subcritical flows (Bowen et al, 1984; Dorrell et al, 2013; Pirmez & Imran, 2003). As shown by the aforementioned paradox, there is no connection between stratification for particulate gravity currents and Froude number. This hypothesis is also reinforced by Stevenson et al (2014) that channelized flows quickly create and sustain continuously stratified subcritical flows until stepped stratification profiles are produced by late-stage development of cohesive forces over turbulent forces.

With particle sedimentation balancing turbulent mixing and resuspension, gravity currents naturally have vertical variations in density. This density for turbidity currents is dictated by the amount of sediment in the current. Density profiles have previously been described by three different models:

- I. Two-layer model (Figure 5a) was first introduced by Middleton (1969), and also observed by Middleton & Hampton (1973), Ravenne & Beghin (1983), Mulder et al (1997) in experiments that with a dense lower portion of the current and a low-concentration plume at the top;

- II. Continuous profiles (Figure 5b&d) illustrate a continuous decrease in concentration with increasing height. This model characterizes weakly depositional subcritical flows (Altinakar et al, 1996); low-concentration , depositional subcritical flows in laboratory (Garcia, 1994); and supercritical flows on low slopes in laboratory (Garcia & Parker, 1993). Theoretical models (Stacey & Bowen, 1988) and direct measurement of turbidity currents (Normark, 1989) also reinforced this continuous profile;
- III. Stepped model (Figure 5c) has a region near the maximum velocity, where the intensity of turbulence is reduced and the generation of turbulent kinetic energy is reduced, a proposed dynamic barrier for the sediment transportation from the inner to the outer part (Garcia & Parker, 1993).

The step profile has been observed in subcritical and supercritical experimental flow in where high entrainment rate of ambient flow at the upper part or the sediments were entrained by erosional flows (Garcia & Parker, 1993). Saline flows and low-concentration flow in the laboratory shows continuous concentration profiles. However, a very stepped profile can be seen from direct observations of a salinity gravity current in the southwest Black Sea (Sumner et al, 2014).

2.2.3 Turbulent Mixing

The turbulent structure of gravity currents was first studied experimentally by Kneller et al (1997) using laser Doppler anemometry. Subsequent work includes Buckee et al. (2001), which has recently been revisited by Islam and Imran (2010). Cossu and Wells (2012) used acoustic Doppler velocimetry and showed that the turbulent structure of saline and turbidity currents have no significant differences. An almost consistently observed essential feature is a low level of turbulence near the velocity maximum, with higher levels along the wall in the inner region and in the shear layer in the outer region (Kelly, 2018). This low-turbulence area is known as the slow diffusion zone (SDZ) because it is thought to hinder mass transfer between the inner and outer regions (Buckee et al, 2001; Peakall et al, 2000). The low area of turbulence can be produced by shear or buoyancy. Reynolds stresses and velocity gradient are necessary for shear formation:

$$P_{\text{shear}} = -\overline{u'_i u'_j} \frac{du_i}{dx_j} \quad (8)$$

Stratification, or variation of buoyancy normally, acts to dampen turbulence within a flow (it is harder to lift a comparatively dense parcel of fluid vertically upwards into a region of lighter fluid, where it would naturally want to sink). “Buoyancy production” is dependent on the buoyant fluxes:

$$P_{\text{buoy}} = -\frac{g}{\rho_a} \overline{\rho'w'} \quad (9)$$

But may be assumed to be on average an energy sink, like viscous dissipation, unless the flow is unstably stratified. Due to the zero velocity gradients at the velocity maximum, the shear component is low in magnitude and contributes significantly more to gravity currents (Buckee et al, 2001; Islam & Imran, 2010). Note that prior research, like that of Buckee et al (2001), only documented in the vertical plane and disregarded cross-stream components (i.e. the shear production was determined using just the $u'w'$ term) because of the available technology. Turbulence strength was found to be higher in the cross-stream than in the vertical direction by Islam and Imran's 3D technology, which is why it should be considered in all turbulence computations.

2.3 Partially Confined Turbidity Currents

Being a subset of gravity currents, turbidity currents primarily depend on flow buoyancy to determine their horizontal velocity. They have more complex fluid dynamics than gravity currents, though, because of the levels of turbulence, density stratification, and suspended sediments (Wells & Dorrell, 2021). Turbidity currents are sediment-filled flows that spread throughout reservoirs, lakes (Best et al, 2005; Cossu et al, 2016), and oceans (Mountjoy et al, 2018; Mulder et al, 2003), as a result of their different densities from ambient fluid. One major mechanism for transporting sea floor sediment is the turbidity current, and compared to rivers, the volume of transported material is much larger (Paull et al, 2018). At the boundary of two water masses with different sources, such as fast-flowing floods of turbid water flowing downslope, two oceanic gravity current heads are generated. Due to the density difference relative to ambient fluid, turbidity currents propagate across oceans (Mountjoy et al, 2018; Mulder et al, 2003). The processes of flows travelling down slope gradually builds, through deposition and erosion, seafloor canyon and channel systems that either fully or at least partially confine the flows that build them (Klaucke et al, 1998). These channels, much like sub-aerial

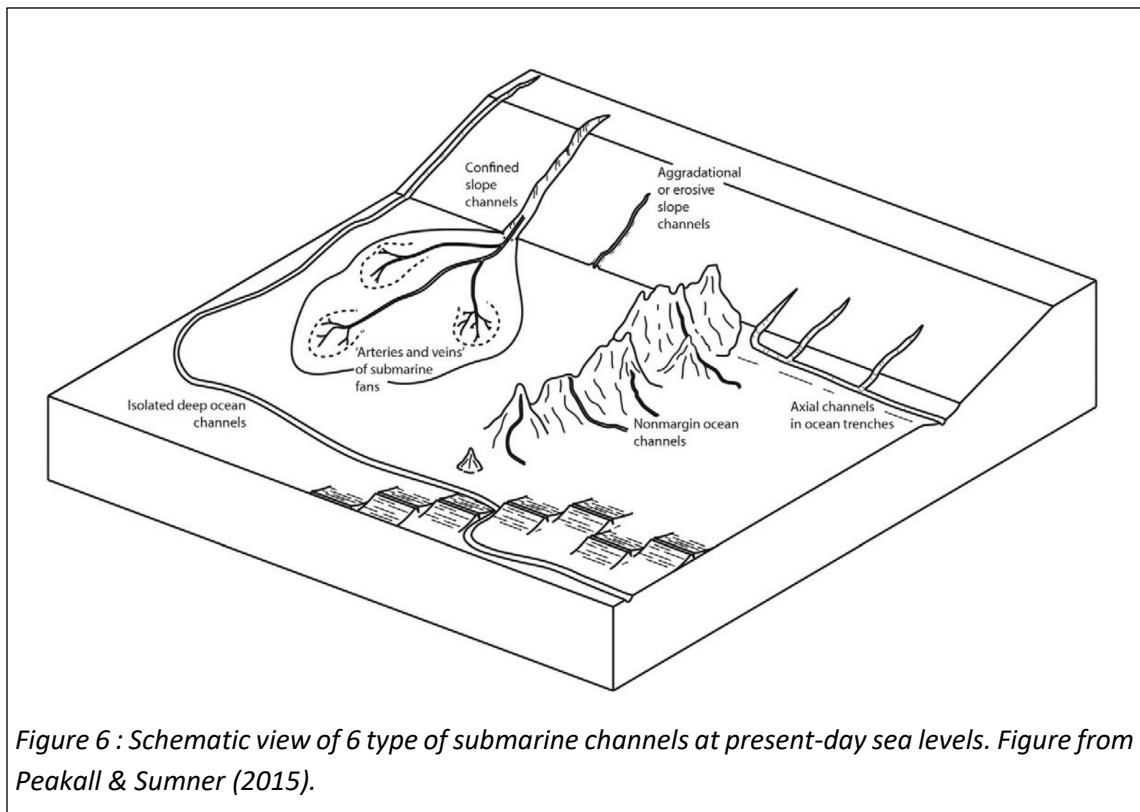


Figure 6 : Schematic view of 6 type of submarine channels at present-day sea levels. Figure from Peakall & Sumner (2015).

rivers meander across the seabed (Lonsdale & Hollister, 1979), concentrating the transport of material over large distances. Indeed, there is such similarity between submarine channels and fluvial systems that they are often referred to as “rivers of the seafloor”. However, these systems can be much larger than terrestrial rivers. Also, fluvial and underwater channel systems have different channel morphology and flow dynamics (Kolla et al, 2001; Kolla et al, 2007; Peakall et al, 2000), with bend migration in submarine channels being significantly reduced (Peakall et al, 2000). The different types of submarine channels at present-day sea levels are shown in Figure 6. Where the characteristic Rossby number, Equation (7), of such systems becomes small these flows are large enough to be affected by rotation of the planet (Simpson, 1999) with increasing latitude. Although flow is mostly contained within the channel, there may be occasional overspill. Large levee systems on either side of submarine channels are frequently present and may even be broader than the channel itself. These levee structures are the result of deposition from flows overspilling the confines of the channel (Birman, 2009; Nakajima & Kneller, 2013). The deposition on inner/outer bank is determined by degree of confinement and Coriolis effect (Cossu & Wells, 2013; Straub & Mohrig, 2008).

The majority of submarine and subaerial channels are moderately to highly sinuous (Langbein & Leopold, 1970; Pirmez, 1994). Since channels are curved, the fluid within them is subjected to centrifugal force that produces cross-stream flow towards the outside bank of bends. The

mathematical formula for centrifugal force (Figure 7) is $mr\omega^2$, where m is the mass of the object, r is the radial distance from the axis of rotation of the frame, and where ω is the angular velocity with respect to the point (Feynman et al, 1965).

2.3.1 A note on Centrifugal Forces

The outward radial force that an object experiences as it moves transversely with respect to a frame of reference is known as a centrifugal force (Weidner, 1975). For instance, because the

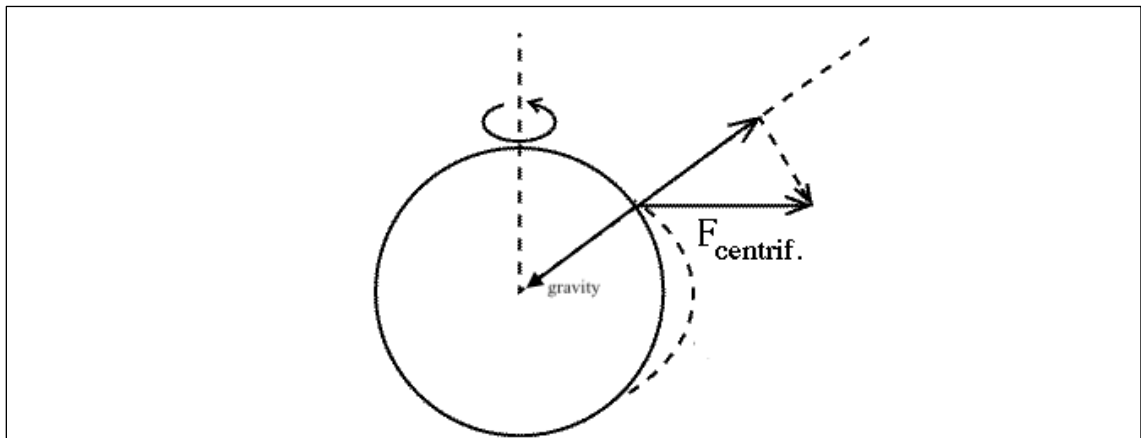


Figure 7 : Schematic illustration of the centrifugal force arising from the rotation of the Earth. Showing gravity always pointing towards the centre of Earth, and the centrifugal force is perpendicular to the axis of the Earth. Note this is distinct from the centrifugal force that can arise from the choice of coordinate system in specific frame of reference, e.g., relative to a sinuous channel traversed by a flow.

Earth spins around a fixed axis, the direction of centrifugal forces always point away from the axis, which is the opposite of the direction that gravity at the equator (Talley, 2011). The curved shape of channels, which provide the dominant centrifugal force, has significant impact on submarine channels.

2.3.2 A Note on Pressure Gradients

All submarine and subaerial flows in meandering channels develop cross-channel superelevation: a cross-stream surface slope that is the leading order balance between the outer bank orientated centrifugal forces. The cross surface slope, and thus pressure gradient force, is largest and most obvious at channel bend apex where centrifugal forces are largest (Rozovskii, 1957).

The degree of cross-channel superelevation controls how much material is lost overbank through overspill. This further defines how channel levees are constructed. There is significant difference between the amplitude of cross-channel superelevation in subaerial and submarine channels; this may be explained due to the reduced density difference of turbidity currents versus rivers compared to respective ambient of water and air (Dorrell et al, 2014).

To study cross-channel superelevation in submarine channels Straub et al (2008) used experiments on 24 turbidity currents driven by $CaCl_2$ and suspended sediment entering a sine-generated channel with three bends to explore how curved channels determine the cross-channel superelevation, deposition and grains size distribution both inside and outside of channels. Straub et al (2008) reported that significant cross-channel superelevation occurred due to run-up at the outer bank resulting in deposition of coarse sediments on the levee crest. In addition, channel relief decreased because of larger deposition at the channel bottom compared to the levee crest.

2.3.3 Flow Dynamics in Sinuous Channels

Both submarine and sub-aerial channel bends exhibit a helical velocity structure with primary and secondary velocity components (Peakall & Sumner, 2015). The primary flow is quite similar to the flow pattern expected if the fluid is inviscid, and the secondary flow is a relatively minor flow superimposed over the primary flow (Figure 8). These areas of secondary flow are typically found close to the fluid's boundary, on solid surfaces where there are viscous forces present, like in the boundary layer.

The dynamics of gravity currents in submarine channels have been explained by considering the comparatively well-studied dynamics of subaerial channels (Rozovskii, 1957) as an analogue. However, super-elevation is substantially larger, by a magnitude of two to three, than subaerial systems because there is a substantially smaller disparity between flow and ambient fluid densities in gravity currents (Dorrell et al, 2013). In order to remain flowing through a bend within the riverbanks, water follows curved streamlines. The water surface is higher near the outer bank than near the inner bank due to the centrifugal force. As a result, there is hydrostatic pressure gradient, resulting in a force directed towards the inner bank. Centripetal forces which are provided by the pressure gradient are necessary for the curved paths (Bowker, 1988). The higher pressure near the outer bank has faster water speed, and the lower pressure near the

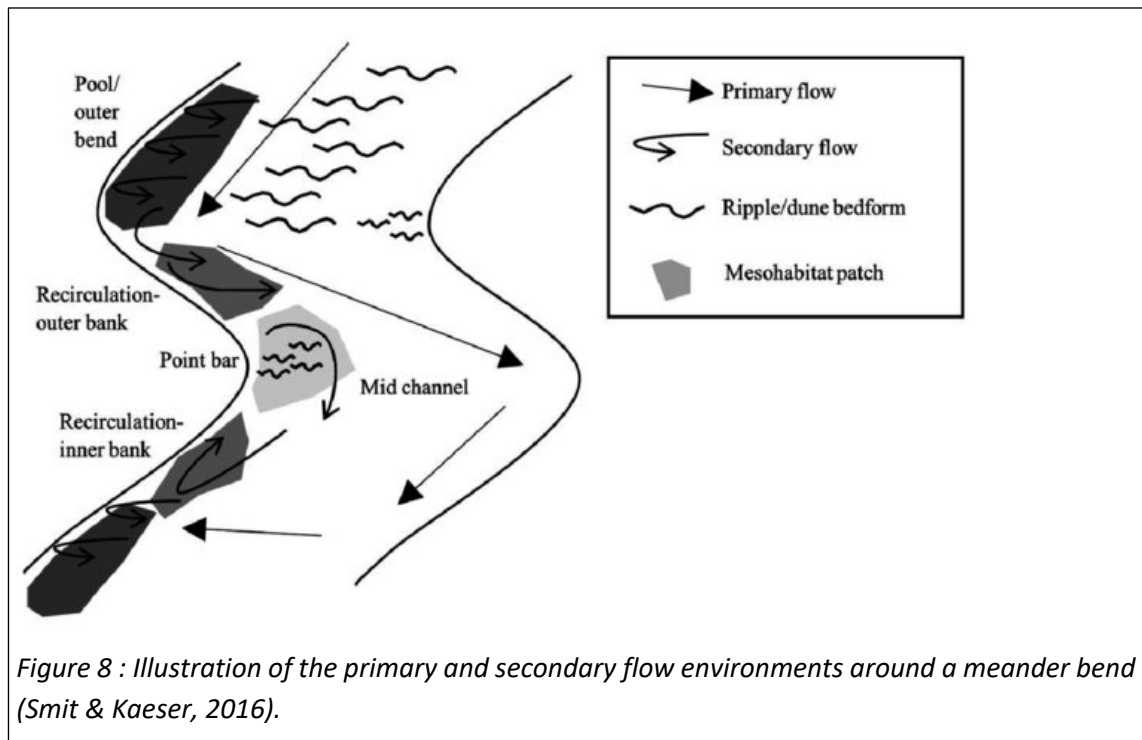


Figure 8 : Illustration of the primary and secondary flow environments around a meander bend (Smit & Kaeser, 2016).

inner bank has slower water speed. Velocity is faster at the near surface, and it moves towards the outer bank; near-bed flow moves in the opposite direction. Velocities toward the outer bank are 3 to 4 times faster than those near the inner bank (Ferguson et al, 2003). A secondary flow forms in the boundary layer along the riverbed. The boundary layer is not able to balance the pressure gradient since it is not moving fast. So, its path is partly downstream and partly cross-stream from the outer bank driven by the pressure gradients toward the inner bank (Dietrich & Smith, 1983).

The direction of the cross-channel plane that delineates the downstream and cross-stream components of flow must be chosen carefully in order to analyse the value and orientation of forces acting in the flow. Unlike laboratory channels in which the cross-section is perpendicular to the walls, the river width is variable in natural rivers with irregular banks. The approach of Rozovskii (1957) determines the mean direction of flow for individual vertical velocity profiles. Then, for each vertical profile, the cross-stream component of velocity is calculated in relation to the mean flow direction. The analysis only produces the secondary circulation and not the whole cross-stream velocity field since the discharge normal to the mean flow direction is taken to be zero. Each vertically averaged velocity is multiplied by the entire depth of flow at the place

of measurement to determine the total cross-stream and downstream discharge measured at each section (Dietrich & Smith, 1983).

Factors controlling secondary flow orientation in submarine channels have been investigated systematically over the years (Abad et al, 2011; Azpiroz-Zabala et al, 2017; Dorrell et al, 2013; Ezz & Imran, 2014; Parsons et al, 2010; Sumner et al, 2014; Wei et al, 2013). Numerical modelling of Kassem & Imran (2004) found secondary flow patterns that matched those of subaerial river channels, with near-bed flow directed towards the inner bank (Imran et al, 2007; Rozovskii, 1957). Yet, in the physical experiments of Corney et al (2006) and Keevil et al (2006) river-reversed secondary flows were seen in which the near-bed flow was directed towards the outer bank. The Froude number and bed roughness serve as significant controls on where the flow velocity maximum occurs, according to Abad et al (2011) , who discovered that both river-normal and river-reversed secondary flows are conceivable. Dorrell et al (2013) addressed this apparent dichotomy systematically by introducing i) radial stratification of the flow: ii) Coriolis force; iii) boundary conditions. Crucially, three-dimensional flow framework assumed that non-zero radial flux boundary conditions are required. Near-bed density flux and the potential for reversed secondary flow can be enhanced by the vertical and radial (horizontal) flow stratification according to the 3-D numerical modelling of Dorrell et al (2013).

Secondary flow is influenced by the equilibrium of centrifugal forces with cross-channel pressure gradients, net cross-channel fluid, and buoyancy flux. Because of this, secondary flow closures do not permit a consistent examination of flow hydrodynamics and, consequently, morphodynamics (Wells & Dorrell, 2021). Secondary flow appears to be temporally unstable according to an analysis of time series data. The number of stacked vertical and horizontal secondary flow cells as well as the direction of near-bed flow both change periodically (Dorrell et al, 2018).

2.4 Latitudinal Control on Turbidity Currents

Submarine channels are one of the conduits for material exchange between shelf and deep ocean: they occur at scales large enough to be affected by the Earth's rotation. The dynamic interplay between turbidity currents and the bottom leads to the development of submarine

channels (De Leeuw, 2016). At high latitudes, the Coriolis force is known to have a significant impact on gravity currents (Akhmetzhanov et al, 2007; Hesse et al, 1987).

Field observation and studies of turbidity currents can be hard and troublesome because such flows occur in the deep oceans, are rare, and potentially destructive. Experimental studies are necessary to study submarine channels because the experimental visualizations illustrate the processes occurring underneath the ocean that are very difficult to observe in the field. Experiments have used rotating flumes to simulate flow deflection from Coriolis force. Clockwise rotation is equivalent to flow in a left-hand turning bend, in the Northern hemisphere, where Coriolis forces are aligned with centrifugal forces. These flows are characterised by a positive Rossby number. Anti-clockwise rotating flow is equivalent to flow in a right-hand turning bend, in the Northern hemisphere, where Coriolis forces are opposed to centrifugal forces. These flows are characterised by a negative Rossby number. In the Southern hemisphere, the relationship between clockwise and anti-clockwise flows and left-hand and right-hand turning bends is reversed.

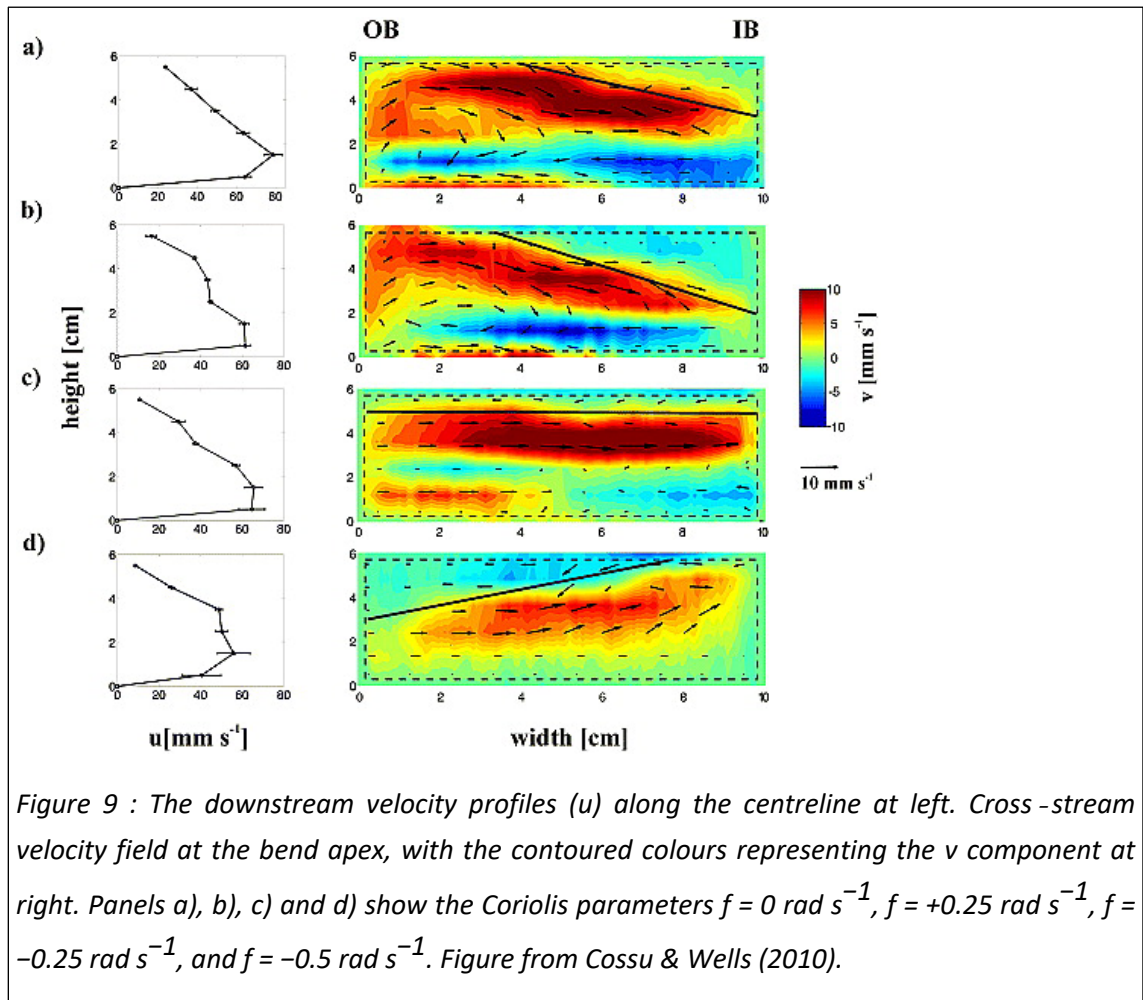
However, experimental research on the impact of Coriolis on the flow dynamics of these channels has largely been restricted to velocity profiles and isolated, low-resolution, two-dimensional cross-sectional velocity fields. Previous experiments on the impact of Coriolis on density currents were also conducted at relatively low Reynolds numbers (Cenedese & Adduce, 2008; Cenedese et al, 2004; Cossu & Wells, 2010; Cossu et al, 2010; Wåhlin et al, 2008). Mixing has been studied over a sloping bottom in a rotating freshwater system (Cenedese & Adduce, 2008; Cenedese et al, 2004). There is a need to explore the dense water and ambient mixing under the influence of Coriolis force in a sinuous channel. This is needed to provide more detailed insights about flow velocity, density and mixing profiles – potential solutions to the auto-suspension paradox, as natural flows occur in sinuous channels not idealised channels predominantly considered previously. Due to the limitation of field data, especially for submarine channels, experimental modelling becomes significantly important for understanding dynamics of gravity currents.

Coriolis forces also affect the velocity distribution in straight subaqueous channels. The Coriolis force has a marked impact on turbidity currents, which are diverted to the right (looking downstream) in the Northern Hemisphere and to the left in the Southern Hemisphere. This causes an asymmetry in the height of overbank levees, with levees higher on the right in the

Northern Hemisphere and on the left in the Southern Hemisphere. This is evidenced in natural systems such as the North Atlantic Mid-Ocean Channel (NAMOC).

Cossu et al (2010) investigated the influence of Coriolis on straight channels with levees using a computer-controlled rotating platform with a saline gravity flow as an analogue of turbidity currents. Both Ultrasonic Doppler Velocity Profiler (UDVP) and Acoustic Doppler Velocimeter (ADV) were used to capture the along-stream and cross-stream velocity. There was also a digital camera placed looking upstream to measure the thickness of the current and slope and deflection of the interface. It was observed that the greatest velocity was found to be between 0.5 and 1 cm above the bed. Between the base and the highest velocity, U_{max} , in the bottom boundary layer, the velocity rose nonlinearly. Above that, it decreased continuously. With positive f , the current deflected to the right; for negative f , the current deflected to the left. The deflection became more significant with increasing rotation rate. The downstream velocity decreased with the increase of rotation rate. From the across-stream velocity profile, two

neighbouring flow cells in the channel rotated in opposite directions while remaining stationary, with the density current convergent at the surface and divergent at the bottom.



By controlling the secondary circulation of turbidity currents, it is hypothesised that the combination of centrifugal and Coriolis forces controls the sinuosity of undersea channels. Secondary flow varies with depth; it can be orientated towards the inner bank or outer bank near the bed depending on controls like overspill (net radial material transport) (Dorrell et al, 2013). In the Northern Hemisphere, it has been noted that Coriolis forces divert gravity currents to the right, which results in overbanking sediment flows on the right side (looking downstream) for mid- and high latitudes. In the southern hemisphere, it is the opposite (Cossu & Wells, 2010).

Cossu & Wells (2010) conducted a comprehensive set of experiments to investigate the effects of Coriolis force on sinuous channels, by investigating different rotation rates, to investigate the mutual interaction of these forces on the flow dynamic. The findings demonstrate that, in the

absence of rotation, centrifugal acceleration causes the density interface to slope upward in the direction of the outer bend (Figure 9a). As a result of the Coriolis force operating in the same direction for $f=0.25$, $R_o=0.55$ the interface tilted more toward the outer bend, however for $f=-0.25$ $R_o=-0.42$, the Coriolis force opposes centrifugal force causing the super-elevation at the outer bend to be greatly reduced. The Coriolis and centrifugal forces were balanced at $0.35 < R_o < 0.45$ and the interface in the bend apex was almost horizontal.

From the velocity profile (Figure 9), it is clear that there is a development of secondary circulation at the channel cross section. For non-rotating experiments ($f=0$, Figure 9a) the current flowed from the inside bend (IB) to the outside bend (OB) of the bend near the base while above this, it flows from the outside to the inside bend, causing upwelling near the outer bank. For $f=0.25$, the flow resembles a non-rotating experiment in terms of its structure. Yet, there is a rise in super-elevation at the outer bend when the Coriolis and centrifugal effects on the flow are equal in strength (Figure 9b). For $f=-0.25$ and $f=-0.5$, the flows toward the outer bend has decreased significantly, but there was still a flow between 3-5cm directed to inner bend because the opposition of centrifugal and Coriolis forces suppressed the height difference in the outer bend and inner bend. These experiments do not investigate the effect of Coriolis force on the mixing mechanism between the turbidity current and the ambient water.

Turbidity currents and the seafloor interact dynamically, leading to the development of submarine channels (De Leeuw, 2016). Kane et al (2008) found that deposition at channel bend is impacted by the system's degree of bypass, which is related to channel aspect ratio (width divided by height). Cossu & Wells (2013) conducted an experimental study with varying Coriolis parameters ($f= 0, +0.5, -0.5 \text{ rad s}^{-1}$) in a channel has straight and sinuous components. There is a chance that combination of aspect ratio and Coriolis force affect the mixing between density current and ambient water, but there is no study available in the literature that would explain this aspect.

2.4.1 Ekman Layers

Ekman layers are fluid layers where the pressure gradient force, turbulent drag and Coriolis force are balanced (Ekman, 1905). Ekman layers can form on the ocean's surface where surface winds drag the water, as well as at the ocean's and atmosphere's bottom where frictional forces are brought on by the flow over rough surfaces (Ekman, 1905). The mathematical solution for the structure of the Ekman layers was developed by Ekman (1905). Stuart (1954) and Gregory &

Walker (1960) noted Ekman layer instabilities over a constant rotation, however, detailed description of the transition to turbulence for a rotating boundary layer with Ekman layer instabilities was first provided by Faller (1963). Ekman boundary layers are known to be produced by Coriolis forces in gravity currents (Wåhlin, 2004). In the boundary-layer of gravity flow that travels downstream, it has been demonstrated that Ekman boundary layers are essential for controlling the rotationally controlled secondary circulation (Cossu et al, 2010; Wåhlin, 2004). Coriolis forces will produce strong Ekman boundary layers if the Rossby number is low. The thickness of the Ekman layer, δ_E , depends on the viscosity of the fluid and the rotation rate (Cossu et al, 2010).

Ekman boundary layers are essential for determining the rotationally controlled secondary circulation in the gravity flow boundary layer that flows downstream. Coriolis forces will produce robust Ekman boundary layers if the Rossby number is low.

2.5 Summary

According to the literature review study, the research of flow velocity, density, turbulence and entrainment all comes from studying idealised gravity currents in straight channels. However, real-world systems are much more complex and there is a need to understand the dynamics of gravity currents in systems that more closely resemble real-world settings in order to attempt to explain the auto suspension paradox.

In real-world systems, submarine channels are mostly sinuous and are affected by the Earth's rotation. Therefore, the mixing of gravity currents with ambient flow must consider the impact of both centrifugal force and Coriolis force. In the previous literature review, there is more and more study on density currents (Abad et al, 2011; Amy et al, 2005; Azpiroz-Zabala et al, 2017; Benjamin, 1968; Cenedese & Adduce, 2008; Dorrell et al, 2018; Dorrell et al, 2013; Dorrell et al, 2014; Dorrell et al, 2019; Ellison & Turner, 1959; Griffiths & Linden, 1982; Imran et al, 2007; Islam & Imran, 2008; 2010; Kelly et al, 2019; Kneller et al, 1997; Kneller et al, 1999; Marshall et al, 2021b; Maslin et al, 2006; Middleton, 1966b; Parker, 1976; Parker et al, 1986; Peakall et al, 2001; Peakall et al, 2000; Piper & Deptuck, 1997; Sequeiros et al, 2010; Simpson, 1972; 1999; Sumner et al, 2014; Sumner et al, 2013). It is now known that Coriolis force have significant influence on dynamics of gravity currents in the channels under the sea. The influences on flow deflection and velocity have been studied in recent years (Cossu & Wells, 2010; Cossu & Wells, 2013; Cossu et al, 2010; Davarpanah Jazi et al, 2020). It is also important to understand how

Coriolis affects the mixing of shelf-ocean water since this is the main process of material transport and carbon cycle: how does Coriolis forces influence mixing at the gravity currents and ambient fluid at the interface above the body? This key question has not been answered. To understand the physical processes, one of the important points we must investigate is how Coriolis forcing affects the dynamics of gravity currents.

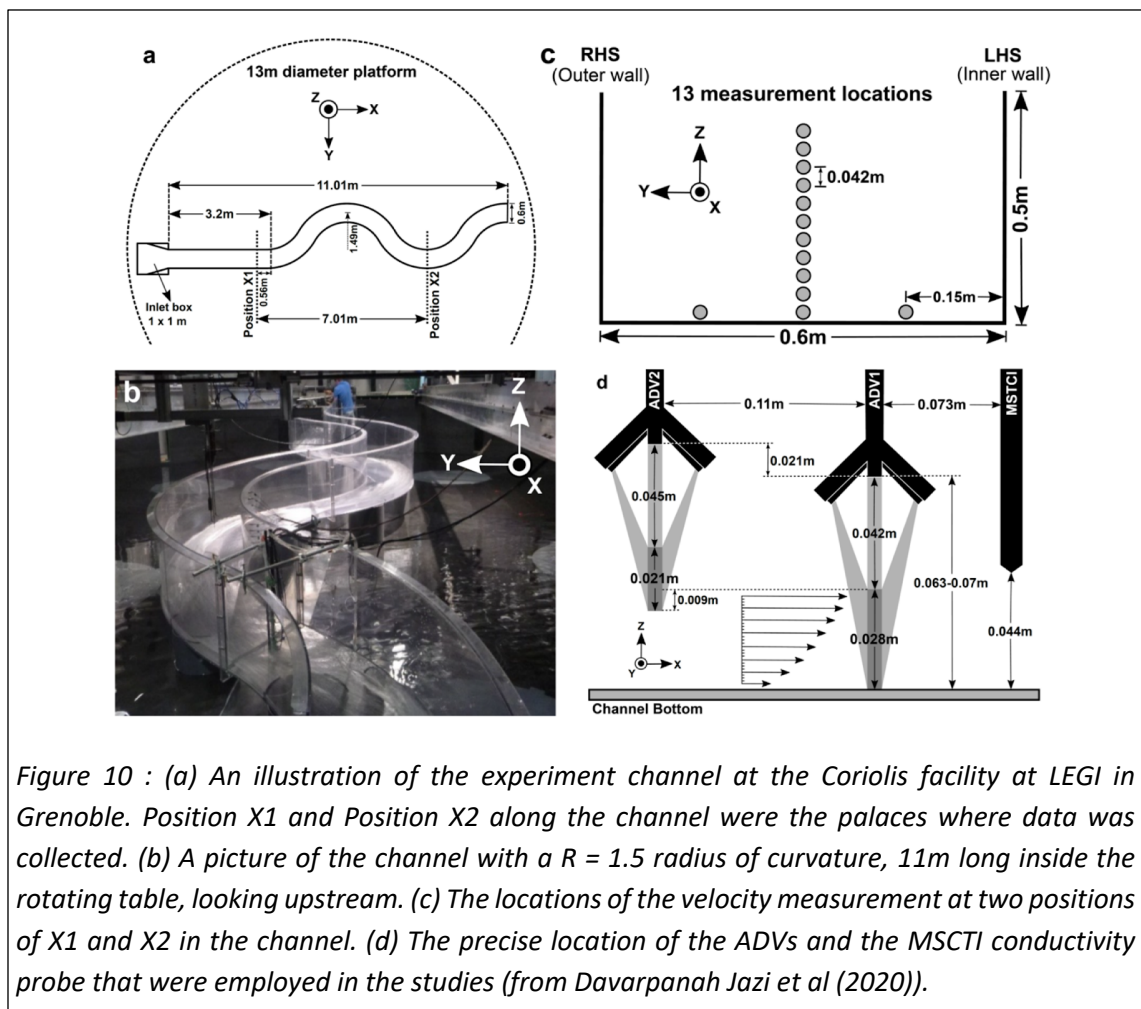
There are other environmental controls that effect the dynamics of the flow along with the Coriolis. For example, the effect of channel width-depth aspect ratio, especially when subject to Coriolis forcing, may affect the mixing between density current and ambient water. However, there is no study available in the literature exploring this yet. This thesis therefore expands on existing work looking at Coriolis force on secondary flow dynamics, to consider implications for flow mixing. Potential further work is left for the discussion.

Chapter 3 Methodology

3.1 General description of the experiments

The submarine channel experiments described in this thesis were carried out in 2016 by Jeffrey Peakall, Stephen Darby, Robert Dorrell, Robert Thomas, Shahrzad Davarpanah Jazi, Gareth Keevil, Mathew Wells, Joel Sommeria, Samuel Viboud at the 13 m-diameter CORIOLIS II at Laboratoire des Ecoulements Geophysiques et Industries, Grenoble, France, which is the largest rotational flume in the world. These experiments looked at the dynamics of the heads of gravity currents in sinuous channels with changing Coriolis forcing.

Within the Coriolis facility, a submarine channel model was placed. The channel was 11-m long, 0.6 m wide and 0.5 m high with a slope of $3/50$ radians (3.5 degrees, 6% gradient). The channel was positioned in the large tank consists of an initial tapered input section, contains a straight



channel section of 3.2 m, and two bends with a mid-channel radius of 1.5 m sinuosity of 1.2. Figure 10 shows the schematic and photograph of the channel. In order to simulate a turbidity current, saline water was pumped into the top of the channel. The fluid, in turn, can then be brought down in one of two ways: either while being recirculated, with a maximum flow rate of $20 \text{ m}^3/\text{hr}$ (5.55 l/s), or by being emptied down a drain, which any flow rate is possible.

An experimental coordinate system is defined in Figure 10. When the traverse is at position X1, the basal ADV probe (ADV1) is positioned at a position 0.56 m upstream from the downstream end of the straight channel, where X is specified as zero. At the second apex and 7.01 m downstream of position X1, position X2 was assigned.

3.2 Experimental Parameters

The tank was filled with 1 m depth of fresh water and the experiment was carried out at least 12 hours after the ambient was rotated to a solid body rotation. The tank was rotated in different rates and different direction (clockwise or counterclockwise) to form different Rossby numbers and simulate the rotation of Northern and Southern Hemispheres. Rotational rates, Ω , between -0.167 and $+0.167 \text{ rad s}^{-1}$ were used in a total of 46 experiments, which included 11 Rossby situations at two places along the channel. The first 18 experiments were test experiments, where Rossby numbers were either infinity and +1. The remaining 28 experiments compose the main experiments discussed herein. The tank was drained, washed and cleaned after the first 18 test experiments. Based on the test experiments, siphon location was recalibrated and new, taller, for the stream-wise UVP probes were constructed and installed. When the calibration of both conductivity probes was being finished, a new traverse sequence was also developed. These works were to ensure all of the flow was captured in the main experiments.

The saline water was allowed to run for 15 minutes before the data were collected since at this point the flow density at the measuring points had stabilized. Table 1 below lists specifics of fixed and variable parameters.

<i>Table 1 : Range of fixed and variable flow parameters for the experiments.</i>		
Parameters	Definition	Values
Q_{input}	Input discharge	5.7-5.9 Ls^{-1}
$\Delta\rho$	Input density difference	18.8 – 20.9 $kg\ m^{-3}$
W	Channel width	0.6 m
ν	Viscosity	$10^{-6}m^2\ s^{-1}$
S	Slope	3.5°
T	Fluid temperature	21 - 22 °C
H_c	Channel height	0.5 m
t	Duration of experiments	900 s
H_w	Water depth	1-1.1 m
Q_{output}	Output flow rate	5.5 Ls^{-1}
R	Centreline radius of curvature	1.49 m
h	Depth of gravity current	0.2-0.4 m
U	Mean downslope velocity	0.1-0.15 $m\ s^{-1}$

Details of the 28 experiments conducted are specified, by date order conducted in Table 2. The names, 'fix', 'rot', 'str1', 'apex 2', refer to the non-rotating fixed cases, the rotating cases, the first straight position (X1), and the apex of bend 2 (X2), respectively. Numbers referred to the date when the experiment is conducted, for example, 0410 refers to October 4th, 2016. The last alphabet refers to the sub-experiments on that date.

<i>Table 2 : Experimental flow conditions.</i>					
Exp. number	Experiment name	Rotation rate	Rossby number	Notes	Used in this study
		rad s ⁻¹	Ro _w		
The tank was drained, washed, cleaned and refilled with fresh water					
18	fixstr1_0410a	0	∞		Siphon , UVP
19	fixapex2_0410b	0	∞		No
20	rotstr1_0510a	+0.083	+1		Siphon , UVP
21	rotapex2_0510b	+0.083	+1		No
22	rotstr1_0610a	+0.167	+0.5		Siphon , UVP
23	rotapex2_0610b	+0.167	+0.5		No
The tank was drained, washed, cleaned and refilled with fresh water					
24	rotstr1_1010a	+0.041	+2		Siphon , UVP
25	rotapex2_1010b	+0.041	+2		No
26	rotstr1_1010c	+0.021	+4		Siphon , UVP

27	rotapex2_1010 d	+0.021	+4		No
The tank was drained, washed, cleaned and refilled with fresh water					
28	rotstr1_1210a	-0.083	-1	The fire alarm distracted which cause the 4th set of siphon samples (t = 20 min) were not collected	Siphon , UVP
29	rotapex2_1210 b	-0.083	-1		No
30	rotstr1_1310a	-0.041	-2		Siphon , UVP
31	rotapex2_1310 b	-0.041	-2		No
32	rotstr1_1310c	-0.021	-4		Siphon , UVP
33	rotapex2_1310 d	-0.021	-4		No
34	rotstr1_1410a	-0.0104	-8	Ambient was too salty	Siphon
35	rotapex2_1410 b	-0.0104	-8	Ambient was too salty	No
36	rotstr1_1710a	-0.0052	-16	Ambient was too salty	No
The tank was drained, washed, cleaned and refilled with fresh water					
37	rotstr1_1810a	0	∞	The primary goal was to gather PIV data and capture a high-quality movie	No

38	rotapex2_1810 b	+0.0104	+8		No
39	rotstr1_1910a	+0.0104	+8		Siphon , UVP
40	rotapex2_1910 b	-0.0104	-8		No
41	rotstr1_1910c	-0.0104	-8		UVP
42	rotstr1_2010a	-0.167	-0.5		No
43	rotapex2_2010 b	-0.167	-0.5		No
44	rotstr1_2010c	-0.167	-0.5	The main goal was visualization and movie shoot	No
45	rotstr1_2110b	-0.083	-1	The main goal was visualization and movie shoot	No

From the 28 experiments, 12 sub-experiments ending with b and d were not reported in this study because: for these experiments, from 15 to 30 minutes after the experiment began, only ADV measurements were taken at the second apex (Position X2). Seven sets of siphon samples, each lasting a minute, were taken for experiments ending in a and c at intervals of 5, 10, 15, 20, 25, 30 and 35 minutes after the experiment started. From 5 to 15 minutes, the cross-stream UVP data was collected, and from 25 to 35 minutes, the down-stream UVP data. Experiments 37, 45 and 45 were not reported because they were conducted for visualization purpose, and no siphon or UVP data were collected. Experiment with Rossby number -16 is not used because 1) the ambient water got too salty, and 2) there is no corresponding experiment as $Ro = +16$. Experiments with $Ro = \pm 0.5$ were not used in this study. For the case of $Ro = -8$, because of the ambient water got too salty for experiment 34, that made the data from this experiment not valid, however, experiment 41 ($Ro = -8$) is missing Siphon data from experimental notes, only UVP data from this experiment is used in our study.

3.3 Instrumentation and Data Acquisition

Two ultrasonic systems, Ultrasonic Velocimetry Profiling UVP and Profiling Acoustic Doppler Velocimetry ADV, were utilized in experiments to assess velocity. In our study, we used only UVP data for further interpretation on velocity. A single component of velocity can be measured using the ultrasonic velocimetry profiling (UVP) approach at up to several hundred points along a line. An ultrasonic pulse is transmitted via a transducer, which then gates the return signal into a number of spatial bins. For the purpose of gathering downstream velocity profiles, a system of ten 4 MHz UVP probes (with 10 m long cables) was employed. In the studies, probes were positioned 10, 25, 50, 75, 100, 150, 200, 250, 350, and 450 mm above the channel's base. The probes are initially placed on the channel centreline, 80 mm downstream of the bend 2's apex and facing upstream. The nature of secondary flow at the second bend apex as well as the cross-section measurements are investigated using an array of ten 2 MHz UVP sensors (with 4 m long cables). These probes were positioned 45, 90, 135, 180, 225, 270, 315, 360, 404, and 450 mm above the base of the channel.

Fluid samples were taken from the siphon rig throughout the currents in order to collect density data. A custom density siphon created especially for this research was used to extract these samples. The siphon rig consists of 12 siphon tubes, which are secured in the channel portion by a plastic holder that is connected to a rod fastened to the channel. Positioned horizontally 78 mm off-axis from the UVP, the siphon rig is 80 mm downstream of the inflection downstream of bend 2 (on the right-hand side as looking downstream). A height of 10, 25, 50, 75, 100, 125, 150, 175, 200, 250, 350, and 450 mm above the bed was where the siphons were placed. Starting at 5, 10, 15, 20, 25, 30 and 35 minutes into the test, samples are taken over a 60 second interval in a variety of 12 plastic containers. The transit time of fluid moving through the siphons was measured using dye.

In contrast to how the traverse is immediately connected to the Coriolis control software, the UVP and Siphon data are independent as their outputs are not directly tied into the Coriolis control software. The siphons start after 5 minutes, and the cross-stream UVPs start at 5 minutes (run until 15 minutes), and the downstream UVPs start at 25 minutes and run until 35 minutes.

Chapter 4 Results

The analysis of the data collected during the experiments described in Section 3 is presented here. In particular, the time evolution of the flow density and flow velocity are presented, and it is discussed how these profiles are affected by centrifugal and Coriolis forces. Time-averaged downstream velocity profiles and density profiles at the centreline and cross-stream profiles at second bend of channel are shown below. [Here we show that the temporal evolution of the buoyancy and velocity fields of density-driven flows is interlinked, and essential to understand flow dynamics. Previous studies \(e.g. Davarpanah Jazi et al \(2020\)\) have not considered how flow evolves over time, this may distort understanding of key physical process including shear, stratification and turbulence.](#)

4.1 Density Profiles

The density difference, i.e., buoyancy, between the saline gravity current and the fresh water ambient in the experiments provides the force to drive the flows down slope. Therefore, buoyancy is a key control on flow dynamics. Here, the buoyancy parameter is calculated for different conditions of Rossby number. Buoyancy is calculated at the second bend apex as $B = \frac{\rho_f}{\rho_a} - 1$ (Figure 10), where ρ_f is the measured density of the flow and ρ_a is the measured density of the ambient fluid. When the buoyancy parameter tends to zero, it means that the sampled fluid has the same density as the fresh water of the ambient, can therefore be assumed to be the ambient fluid, and is not mixed with the dense fluid flowing in the channel.

Time-averaged density profiles at the second apex of the channel are displayed in Figure 11. The profiles are reported every 5 minutes from 5 to 35 minutes of simulated flow. The case of zero rotation is reported in Figure 11-a ($Ro = \infty$), left panels (Figures 11-b, d, f, h) represent rotation in the clockwise direction and right panels (Figures 11-c, e, g, i) represent are rotation in the anticlockwise direction. The rotation rate increases from top to bottom (i.e., Ro decreases in magnitude from top to bottom).

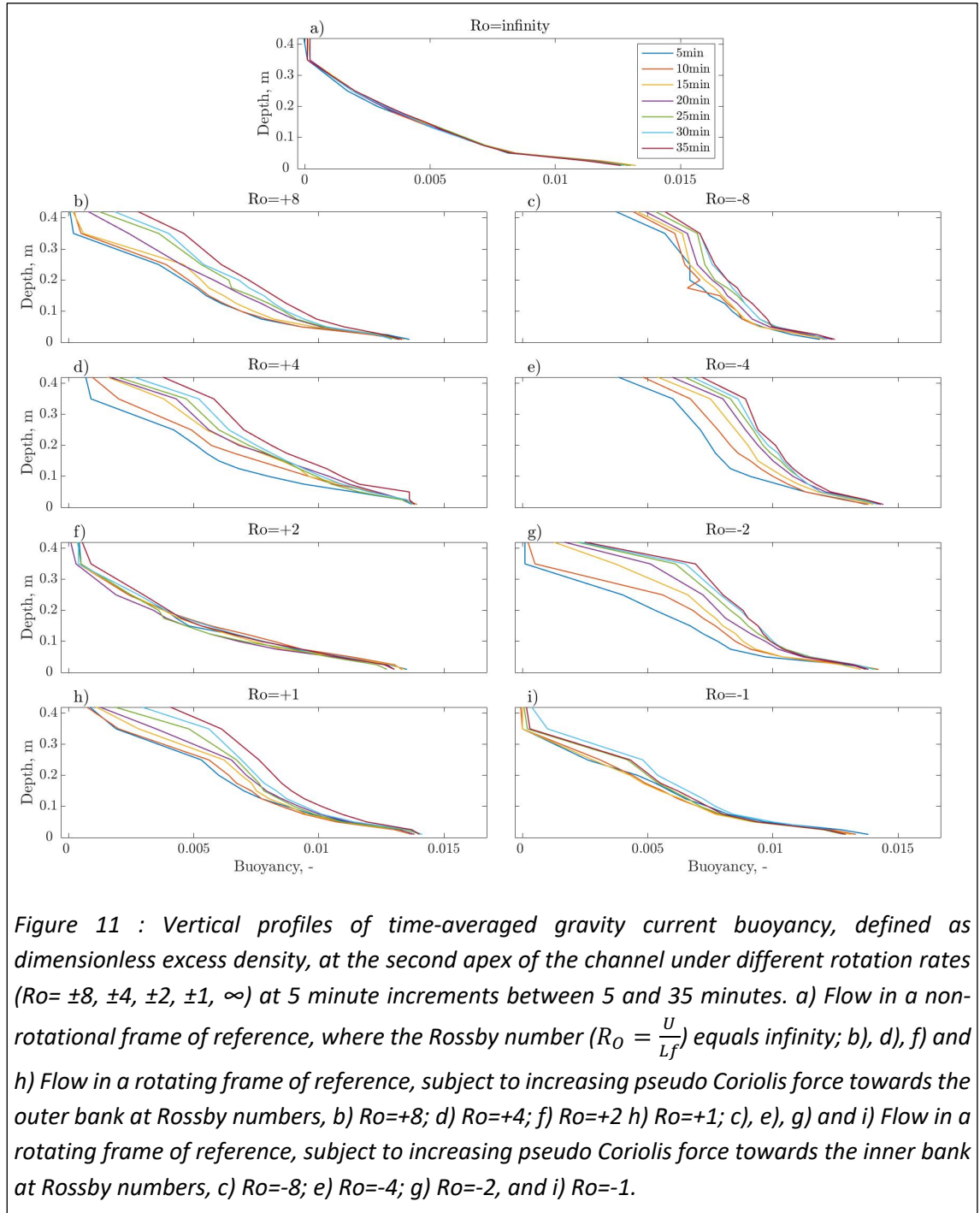


Figure 11-a shows the no rotation case. The current is well stratified, with no excess density above a depth of 0.35 m and an excess density >0.075 in the lower 0.05 m of the flow, and this

does not change with time. **Error! Reference source not found.**s 11-b, d, f, and h, which represent the clockwise rotation cases ($Ro > 0$), show that in most cases, the gravity current gets more mixed with ambient fluid over time (Figures 11-b, d, h). This is highlighted by the reduced excess buoyancy gradient in the upper part of the flow because it has mixed with the ambient fluid, and there is no longer a sharp interface between the fresh water and the dense current. In addition, as rotation increases and Rossby number decreases in magnitude, the rate of mixing increases (Figures 11-b, d, h). The difference in buoyancy is significant between a depth of 0.3-0.45m when the flume gets rotated. It is highlighted that the Rossby number, $Ro = +2$ case has a similar buoyancy profile to the case with zero rotation ($Ro = \infty$). This result is treated as an experimental anomaly, especially since the profile for the faster clockwise rotation case ($Ro =$

+1) does not show a similar profile. Possible explanations for this anomaly are left for the discussion.

Figures 11-c, e, g, and i, show the anticlockwise rotation cases ($Ro < 0$), indicate a complex pattern. In contrast to the clockwise rotating cases, as the rotation rate gets faster (Ro decreases in magnitude), the dense fluid is less well mixed with the ambient fluid. Figures 11-c, e, and g suggest again that it takes more time mix if the rotation rate is not fast enough. $Ro = -8$ is the

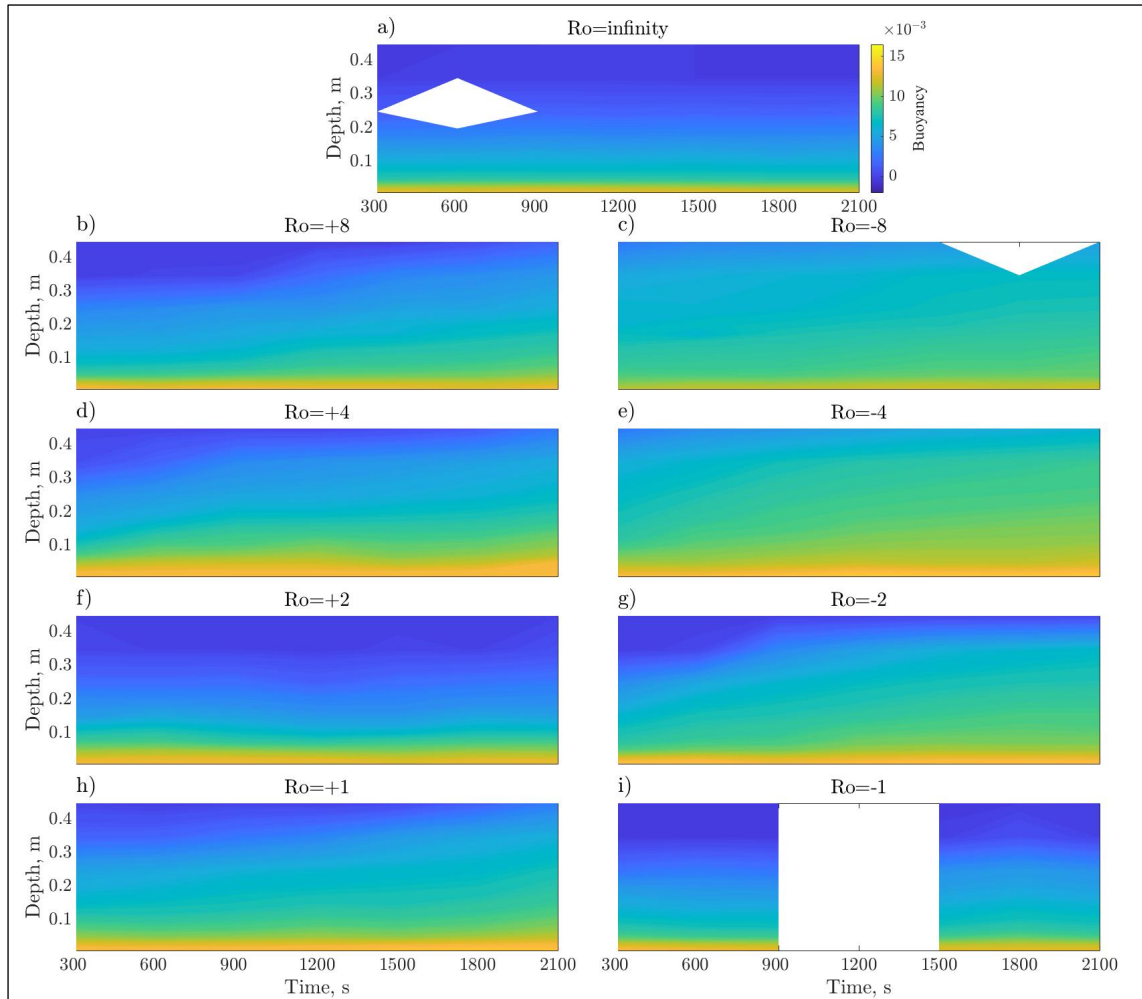


Figure 12 : Contour maps of gravity current buoyancy, defined as dimensionless excess density, at the second apex of the channel under different rotation rates ($Ro = \pm 8, \pm 4, \pm 2, \pm 1, \infty$). a) Flow in a non-rotational frame of reference, where the Rossby number ($Ro = \frac{u}{L_f}$) equals infinity. b), d), f) and h) Flow in a rotating frame of reference, subject to increasing pseudo Coriolis force towards the outer bank at Rossby numbers, b) $Ro=+8$, d) $Ro=+4$, f) $Ro=+2$, and h) $Ro=+1$. c), e), g) and i) Flow in a rotating frame of reference, subject to increasing pseudo Coriolis force towards the inner bank at Rossby numbers, c) $Ro=-8$; e) $Ro=-4$; g) $Ro=-2$, and i) $Ro=-1$.

case when the initial ambient water was very salty (Table 2); such that the results for this case

might not be consistent/comparable with the other anticlockwise experiments. When $Ro = -4$, there is no longer an interface between the fresh water and the dense current. However, when $Ro = -2$, the interface between the fresh water and the dense current can be seen until 15 minutes. It is noted that the fastest negative rotation case reported ($Ro = -1$) also has a similar buoyancy profile to the case with no rotation ($Ro = \infty$) and the case where $Ro = +2$ (compare Figures 11-a, f, i).

Figure 12-a shows evolution of the buoyancy field, driving the flow, with time for the no rotation case. The current is stably stratified since the colour changes uniformly with depth and this does not change with time. This also indicates that no mixing occurs with time. Figures 12-b, d, f, and h, which show the clockwise rotation cases ($Ro > 0$), generally show that as time and rotation rate increase, the region of excess density expands, indicating mixing.

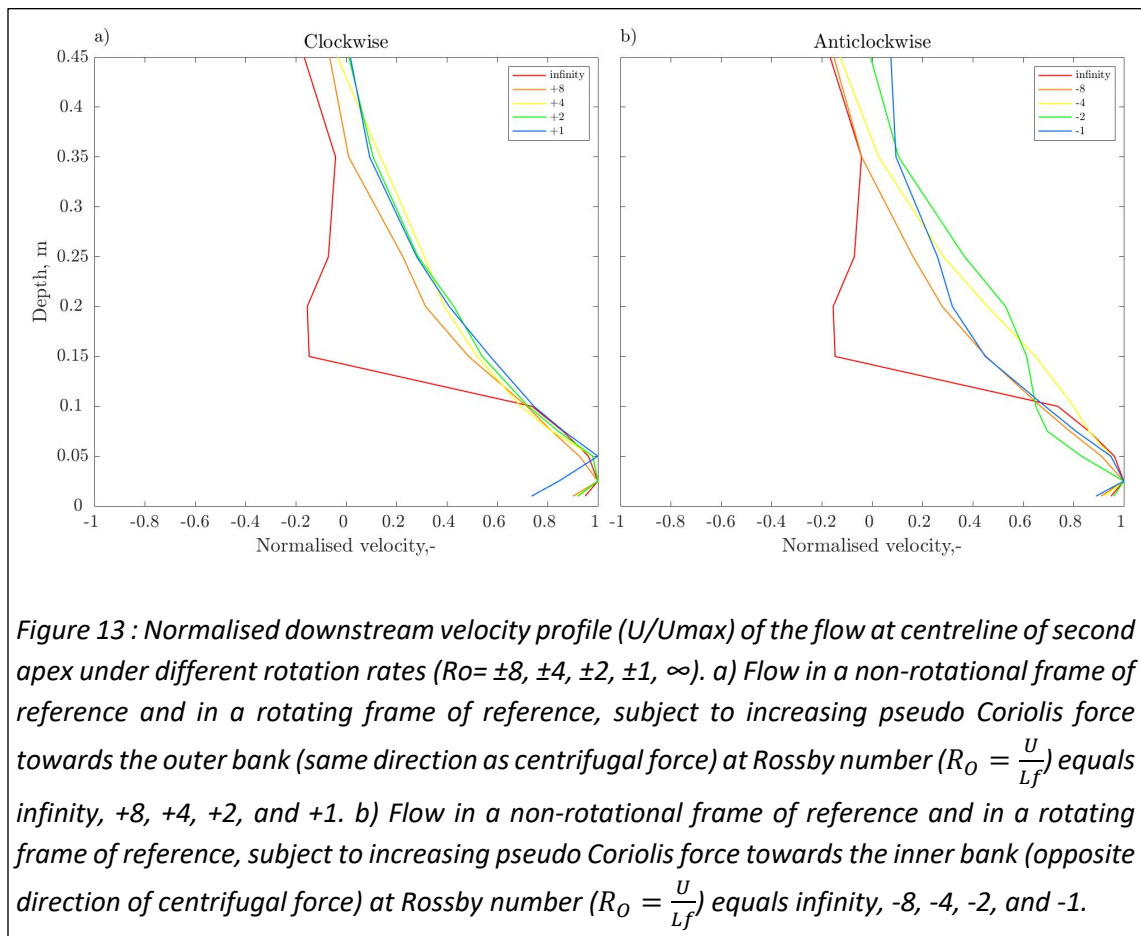
The thickness of the bottom of the current, which exhibits the greatest excess density (shown in yellow), does not change with either rotation or time, which means that the bottom of the current is not significantly affected by rotation or time. The one exception to this pattern is the case $Ro=+2$, which looks like the case without rotation ($Ro=\infty$), similar to the vertical profiles shown in Figure 10-f. In contrast to the clockwise rotation cases, Figures 12-c, e, g, and i, which show the anticlockwise rotation cases ($Ro < 0$), generally show that when the rotation rate gets faster (Ro decreases), mixing decreases. $Ro=-8$ is the case when the initial ambient water was salty and the contour map therefore has almost one colour, suggesting a well-mixed situation with no stratification. However, the $Ro=-4$ case shows a similar pattern, but with a slight trend towards a well-mixed situation over time. When $Ro=-2$, the interface between the fresh water and the dense current can be seen until 15 minutes.

It is highlighted that the fastest rotation case ($Ro=-1$) has a similar buoyancy profile to the case with no rotation ($Ro=\infty$), similar to the vertical profiles shown in Figure 11-i. This is further discussed in chapter 5.

4.2 Downstream Flow Velocity

The buoyancy, or dimensionless density difference, described in section 4.1 drives the flow. The resultant flow velocity is described in this section. Due to no-slip, the flow velocity must be zero at the bed. Also, there is no downslope flow in the ambient fluid, as there is no density difference to drive a flow in this region.

Figure 13 shows normalised downstream velocity of the flow at centreline of second apex of the experiments. In the case of clockwise rotating experiments (Figure 13-a, $Ro > 0$), the normalized vertical velocity profiles have a similar trend. The maximum velocity appears at 0.025 m from the bed for all the other rotation rates ($Ro = +2, +4, +8, 0$), while with high rotation rates ($Ro = +1$, blue line in Figure 13-a) the maximum velocity is located approximately at 0.05 m from the bed. The height of the flow increases with the increase of the rotation of the flume from 0.15 m for the case of non-rotational frame of reference, to 0.35 m for the case of $Ro = +8$, and then it reaches a height that remain constant for all the other simulated rotational cases. Figure 13-b shows normalised downstream velocity of the flow at centreline of second apex for southern



hemisphere. All the anticlockwise cases have a similar trend and have maximum velocity at the height of 0.025m.

Flow velocity is further detailed by looking at the evolution of vertical profiles in time (Figure 14). The case of zero rotation ($Ro = \infty$, Figure 14-a) shows the downstream velocity of the current at depths below 0.1 m is high (> 0.15 m/s) and relatively stable, above that elevation, the velocity decays rapidly but fluctuates intensively.

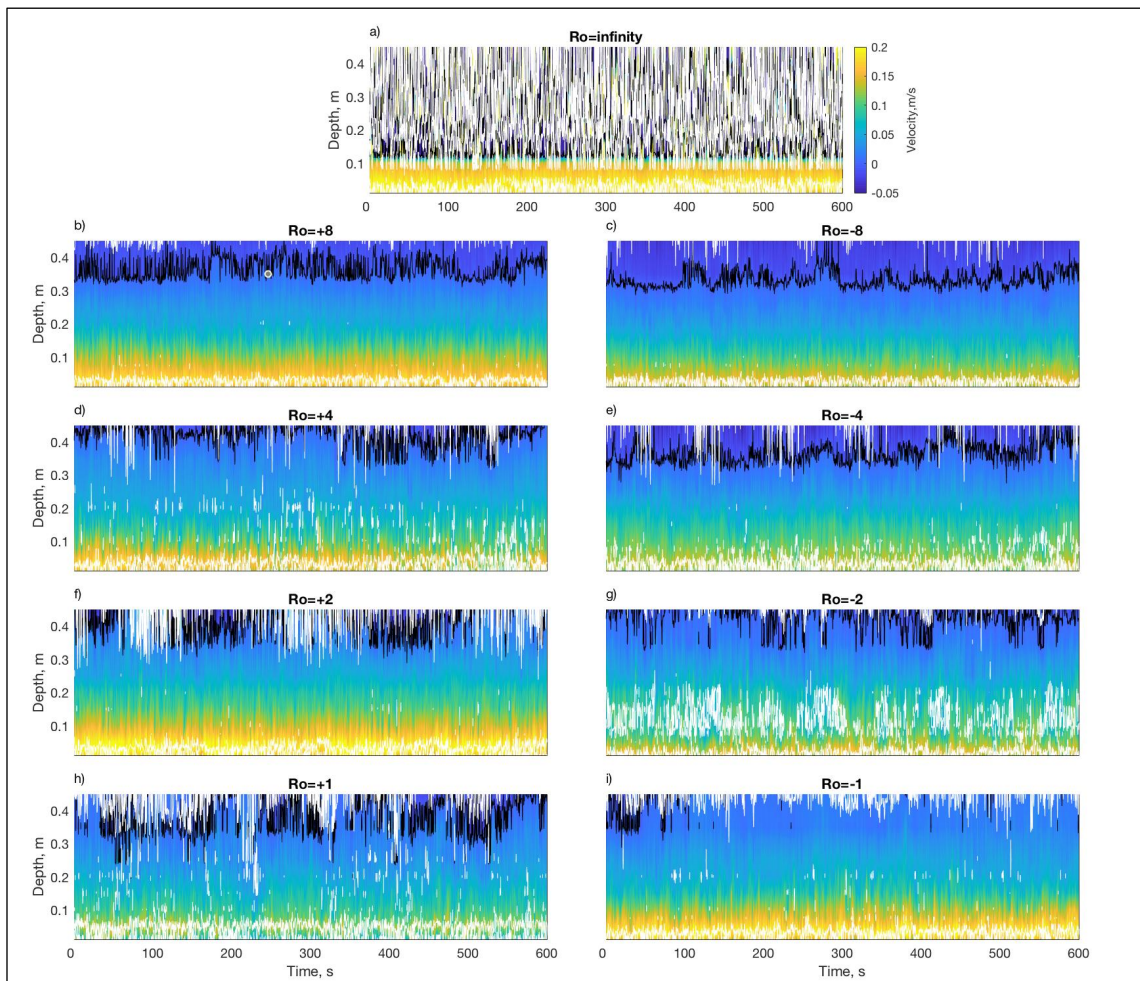


Figure 14 : Contour maps of gravity current downstream velocity at the second apex of the channel under different rotation rates ($Ro = \pm 8, \pm 4, \pm 2, \pm 1, \infty$). a) Flow in a non-rotational frame of reference, where the Rossby number ($Ro = \frac{U}{L_f}$) equals infinity. b), d), f) and h) Flow in a rotating frame of reference, subject to increasing pseudo Coriolis force towards the outer bank at Rossby numbers, b) $Ro=+8$, d) $Ro=+4$, f) $Ro=+2$, and h) $Ro=+1$. c), e), g) and i) Flow in a rotating frame of reference, subject to increasing pseudo Coriolis force towards the inner bank at Rossby numbers, c) $Ro=-8$; e) $Ro=-4$; g) $Ro=-2$, and i) $Ro=-1$. The zero-velocity line (black line) and maximum velocity line (white line) are added to the contour maps.

In general, for rotating flows, the velocity at the bottom gets slower when the rotation gets higher (Ro decreases). The exception to this is case $Ro = +2$ (Figure 14-f). The general trend is because the effect of Coriolis force is more significant when the rotation gets faster, and it suppresses current from moving downstream. The thickness of the region with higher velocity at the bottom also gets smaller with the increasing rotation, which means that there is more mixing between the dense current and the ambient water above. The maximum velocity is located in between 0-0.05m, and zero-velocity is located at upper part around 0.35-0.45m. These plots show that in the case of large values of Rossby number, the high velocity line and zero velocity line are well defined and separated, so that the two zones characterized by maximum (above 0.3 m from the bed) and zero (below 0.05 m from the bed) are well defined and separated.

Whilst Coriolis and centrifugal forces are opposed (Figures 14-c, e, g, i), flow in all cases seems to be well stratified, with clear separation between high velocity near the bed and low velocity above. The contour maps appear to be very similar until Rossby number reaches -1. Only the velocity at the upper part gets bigger with the higher rotation rate. From $Ro = -8$ to $Ro = -2$, the region with higher velocity gets stretched with increasing rotation rate. For the case $Ro = -1$, the rotation is highest in anticlockwise, however, the deflection to the left might not be significant as $Ro = +1$ because the Coriolis and centrifugal works against each other. Maximum velocity is located around 0.025m, and zero-velocity locating around 0.35m for $Ro = -4, -8$, and it is located at more upper with increased rotation rate, which means higher flow height. The zero velocity is located far from the bed, while high velocity is close to the bed, and they are well separated.

4.3 Cross-Stream Flow Velocity

Flow around a fluvial (or submarine) meander bend results in centrifugal force, pushing the flow towards the outer bank. This is balanced by a hydrostatic pressure gradient, generated by a cross-stream water slope, towards the inner bank. However, the net result of variations in flow velocity, and thus centrifugal force, with depth is local imbalances between the two forces. This results in the generation of cross-stream or secondary flow velocity. Cross-stream flow velocity is important as it is responsible for cross-channel sediment transport, and thus meander development and growth.

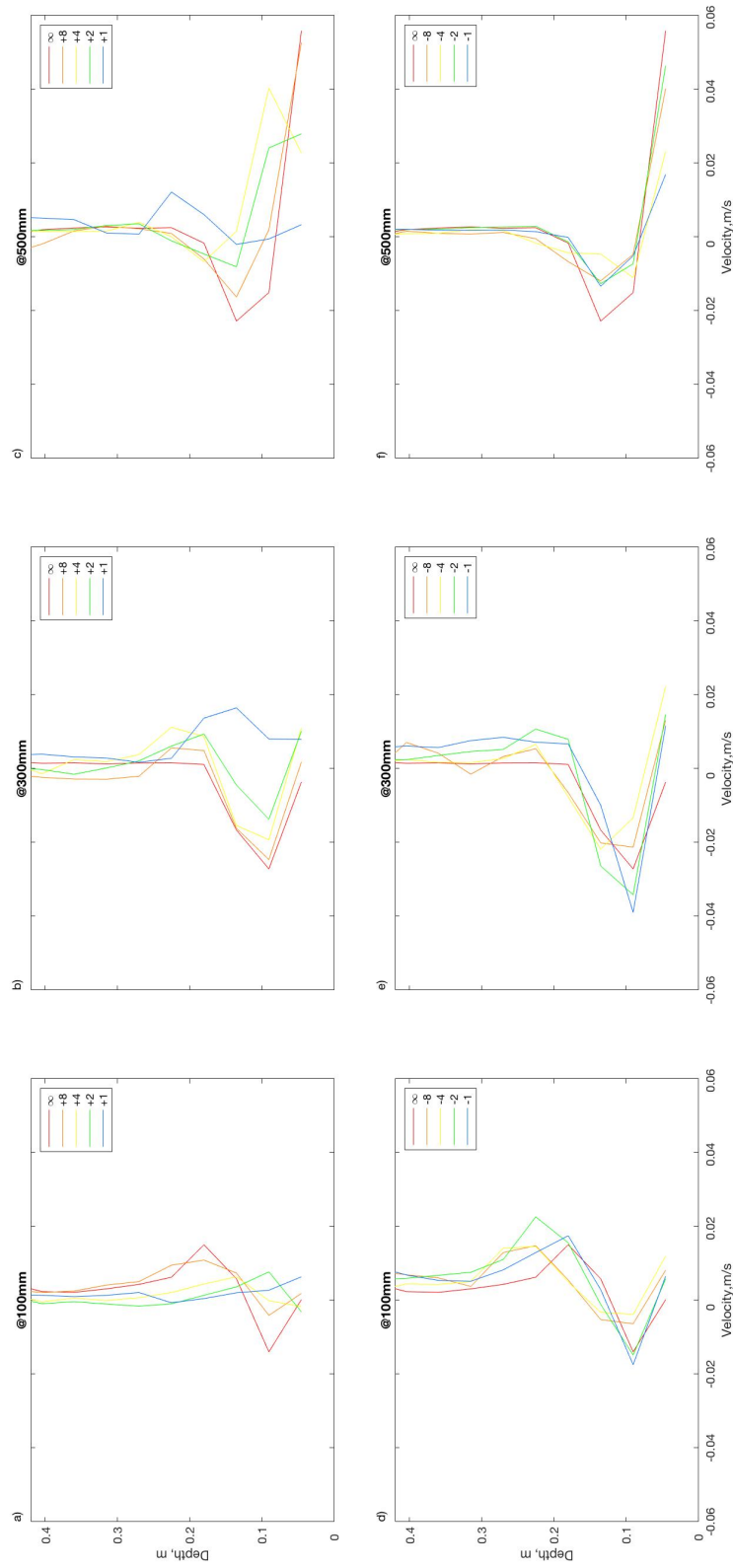


Figure 15 : Cross-stream velocity profile of the flow at three different locations (10cm away from each wall and the centre of channel) of second apex under different rotation rates ($R_o = \pm 8, \pm 4, \pm 2, \pm 1, \infty$). Flow at clockwise rotating frame of reference, subject to increasing pseudo Coriolis force towards the outer bank (same direction as centrifugal force) at Rossby number $(R_o = \frac{U}{L_f})$ equals infinity, +8, +4, +2, and +1 at a)10cm away from left wall, b) at the centreline (channel width is 600mm), c)10cm away from right wall. Flow at anticlockwise rotating frame of reference, subject to increasing pseudo Coriolis force towards the inner bank (opposite direction of centrifugal force) at Rossby number $(R_o = \frac{U}{L_f})$ equals infinity, -8, -4, -2, and -1 at a)10cm away from left wall, b) at the centreline (channel width is 600mm), c)10cm away from right wall.

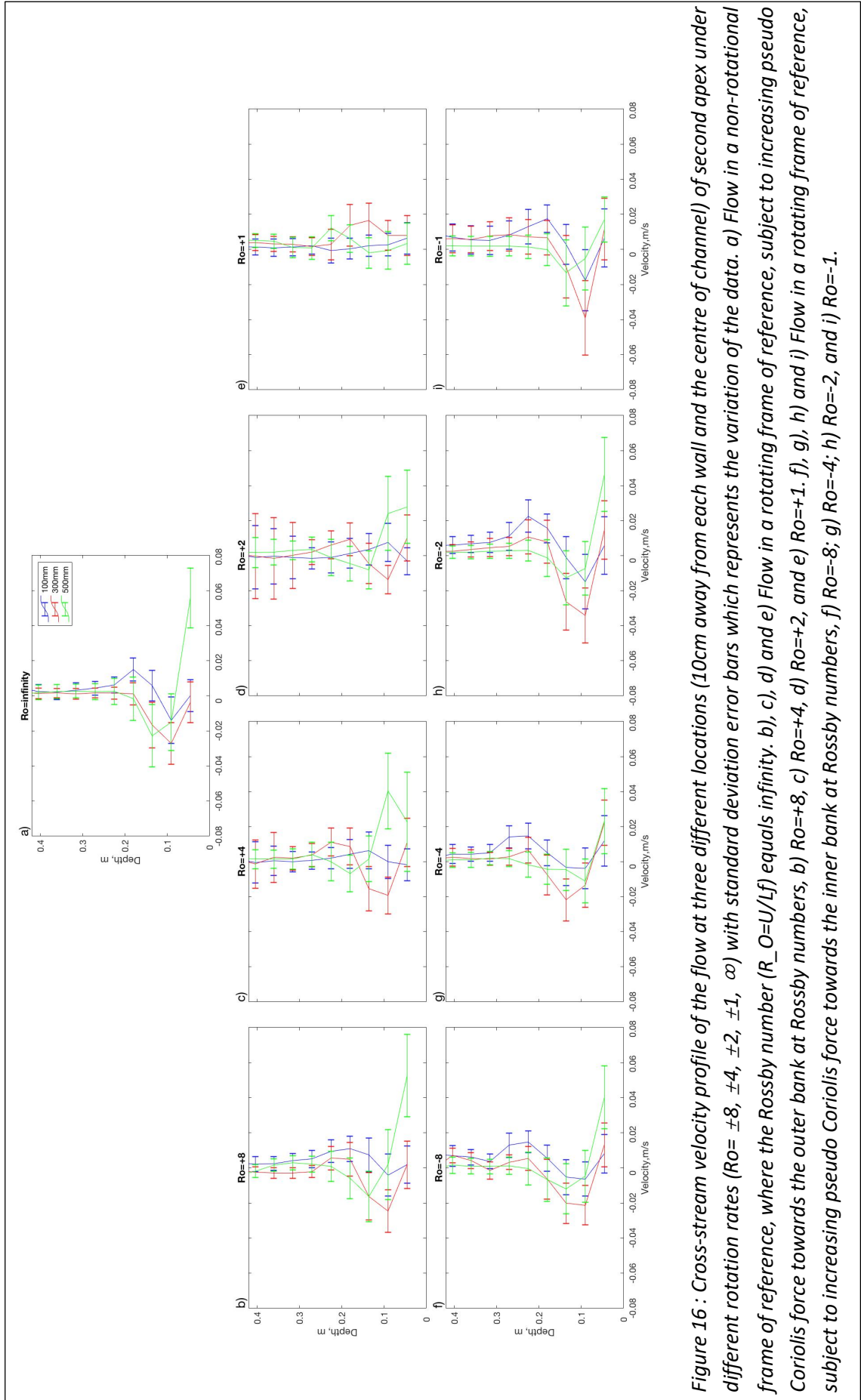


Figure 16 : Cross-stream velocity profile of the flow at three different locations (10cm away from each wall and the centre of channel) of second apex under different rotation rates ($Ro = \pm 8, \pm 4, \pm 2, \pm 1, \infty$) with standard deviation error bars which represents the variation of the data. a) Flow in a non-rotational frame of reference, where the Rossby number ($R_{O=U/Lf}$) equals infinity. b), c), d) and e) Flow in a rotating frame of reference, subject to increasing pseudo Coriolis force towards the outer bank at Rossby numbers, b) $Ro = +8$, c) $Ro = +4$, d) $Ro = +2$, and e) $Ro = +1$. f), g), h) and i) Flow in a rotating frame of reference, subject to increasing pseudo Coriolis force towards the inner bank at Rossby numbers, f) $Ro = -8$; g) $Ro = -4$; h) $Ro = -2$, and i) $Ro = -1$.

Here the cross-stream flow velocity in the meandering submarine channel is detailed. Negative velocity is used to indicate that flow is moving towards inner-bend, where the UVP probes were mounted (Figure 10). Figure 15 depicts the time average cross-stream flow velocity profiles at different distances from the inner bend. Under clockwise rotation (Figures 15-a-c), the flow near the inner bend have almost zero velocity, which can mean that cross-stream movement is not significant, or all of the flow is piled up on the outer bank (away from the UVP) as centrifugal and Coriolis forces are aligned. The $Ro = +1$ case has no cross-stream movement near the inner bend. At the centre of the channel, $Ro=+1$ moves toward the outer bend which is opposite to other slower cases. At the near outer bend location, only the faster rotating case ($Ro= +1$) is moving towards the outer bend.

When the table is rotating anticlockwise (Figures 15-d-f), there is less variation of the cross-section velocity with the increase of the rotation rate. At 100 mm, the cross-stream velocity is zero at the bed, and it becomes negative up to 0.15 m. Moving further from the bed, there is a change in direction of the cross-stream velocity which becomes positive meaning that the flow is moving towards the outer bend.

For the clockwise rotation cases (Figures 16-b, c, d, e), the outer and inner bend cross-stream velocity profiles change with increasing rotation rate and flips over when rotation gets very high. When Ro reaches +4, cross-stream velocity at inner bend (blue line) gets close to zero, when Ro reaches to +1, cross-stream velocity starts to become negative at flow height under 0.25m. Cross-stream velocity at the centreline (red line) is still negative when $Ro = +8$, when $Ro= +4$ and +2 it shows positive between 0.15-0.25m and gets positive below 0.25m when $Ro = +1$. Cross-stream velocity at the outer bend (green line) has positive value between 0.05 and 0.1m and negative between 0.1-0.25 for cases when $Ro= +8, +4, +2$, it becomes nearly zero at $Ro=+1$.

When the table is rotating anticlockwise (Figures 16-f, g, h, i), the cross-stream velocity profile at three locations has a similar trend but the magnitude of the cross-stream velocity is slightly different. The outer bend cross-stream velocity is more likely to be shifted to the right of the figure with increasing rotation rate. The magnitude of cross-stream velocity under flow depth of 0.25m gets larger with increasing rotation rate until $Ro = -2$ and starts to get smaller.

Cross-stream velocity of the flow at second apex of channel is further detailed by looking at the evolution of vertical profiles throughout the channel width (Figure 17). There are two cells showing in the contour map for the case of zero rotation ($Ro = \infty$, Figure 17-a), one is at the

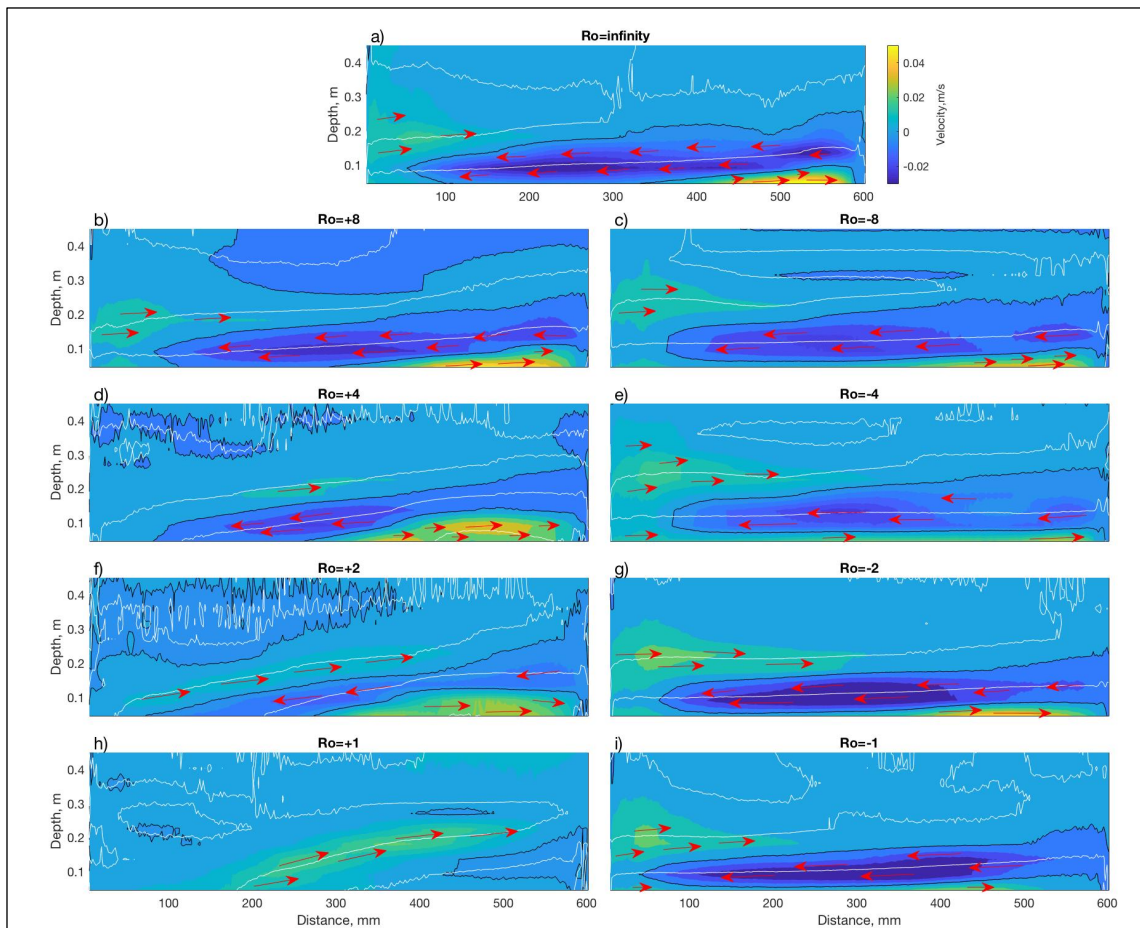


Figure 17 : Contour maps of gravity current cross-stream velocity at the second apex of the channel under different rotation rates ($Ro = \pm 8, \pm 4, \pm 2, \pm 1, \infty$). a) Flow in a non-rotational frame of reference, where the Rossby number ($R_o = U/L_f$) equals infinity. b), d), f) and h) Flow in a rotating frame of reference, subject to increasing pseudo Coriolis force towards the outer bank at Rossby numbers, b) $Ro = +8$, d) $Ro = +4$, f) $Ro = +2$, and h) $Ro = +1$. c), e), g) and i) Flow in a rotating frame of reference, subject to increasing pseudo Coriolis force towards the inner bank at Rossby numbers, c) $Ro = -8$; e) $Ro = -4$; g) $Ro = -2$, and i) $Ro = -1$. The zero-velocity line (black line) and maximum velocity line (white line) are added to the contour maps.

bottom of right-hand side (yellow), one is just above it (dark blue). The “yellow cell” indicates higher velocity that moves towards the outer bend, and the “dark blue cell” indicates movement towards inner bend.

Cross-stream velocity contour maps at the second apex of channel throughout the channel width for 10-minute show an increasing rotation rate in a clockwise direction (Figures 17-b, d, f, h). When there is no rotation, there are two cells showing in the contour map, one is at the bottom of right-hand side (yellow), one is just above it (dark blue). The “yellow cell”, which indicates higher velocity that moves towards the outer bend, moves upward and gets bigger and lighter with increasing rotation rate. That means, the flow at the bottom of outer bend is moving

towards the outer bend, and the cross-stream velocity that moves towards outer bend gets slower with the increasing rotation rate. The “blue cell” gets lighter and diminishes eventually, that means, flow at that height is moving towards the inner bend, and when rotation gets faster it loses its movement towards the inner bend. When $Ro = +1$, there is no “yellow cell” or “blue cell”. The direction of the flow cell at the bottom is anticlockwise and clockwise above that. From the white line, it is easy to see that the current gets more tilted with higher rotation.

For the anticlockwise rotating cases (Figures 17-c, e, g, i), the “yellow cell” gets lighter with increasing rotation rate, except when $Ro=-2$, and diminishes eventually. That means, the flow at the bottom moving towards the outer bend gets slower with increasing rotation rate. The “blue cell” gets flattened with the increasing rotation rate.

Chapter 5 Discussion

Here the results presented in the thesis are summarised and discussed. In particular, downstream flow velocity and density fields are used to assess mixing dynamics, enabling speculation on flow entrainment and turbidity current channel development. Further, experiments are critically reviewed highlighting potential anomalies. This leads to discussion of future work required.

5.1 Time Average Flow Parameters

Flow parameters described in the results section show dynamics of the flow over the 35 minute runtime of experiments (Section 2). Average down stream flow velocity and buoyancy, as function of depth, at the channel centre, are plotted in Figure 18. Average cross stream flow velocity was previously plotted in Figure 15. When the buoyancy parameter approaches 0, it indicates that the sampled fluid has the same density as the ambient water. Mixing between the ambient fluid and the dense current should be low at this sampling position.

The case of zero rotation ($Ro = \infty$, Figure 14a) reveals that the current's downstream velocity was high (> 0.15 m/s) and rather constant at depths below 0.1 m; above that height, the velocity declined swiftly but varied intensely. This suggested a thick flow height of roughly 0.1 m. Further, it suggests that the flow, at this point in space, was not progressively diluted by ambient water, confirming the buoyancy parameter study findings (Figure 12a).

The average vertical velocity and buoyancy profiles in the rotating experiments were different. Whilst the highest velocity was a similar 0.025 - 0.05 m from the bed, both flow velocity and buoyancy decreased much more slowly with depth. Qualitatively the height of the flow grew as the rotation of the flume increased, from 0.15 m for a non-rotational frame of reference to >0.35 m for $Ro = \pm 8$, and then to a height that remained constant for all the other simulated rotational scenarios.

Although a key parameter describing flow dynamics (Wells & Dorrell, 2021), flow depth has not quantitatively been explicitly described within the results. The range of different possible definitions, and interpretations, for flow depth have been left for the discussion. First it is concluded that the Ellison and Turner length scale (Ellison & Turner, 1959):

$$h = \frac{(\int_0^{\infty} u dz)^2}{\int_0^{\infty} u^2 dz} \quad (10)$$

is clearly inappropriate to describe flow depth due to inherent variation in vertical structure within the flow (Figure 13) (Dorrell et al, 2014) and the finite depth of the measurements and ambient fluid (Figures 11-17). There exist three potential dynamic boundary conditions that could be considered to define flow depth. A density boundary condition, where excess flow density buoyancy vanishes,

$$B|_{z=h} = 0 \quad (11)$$

A downstream zero-velocity boundary condition (see e.g. (Dorrell et al, 2014)):

$$u|_{z=h} = 0 \quad (12)$$

A cross-stream zero-shear velocity boundary condition (see e.g. (Abad et al, 2011)):

$$\left. \frac{dv}{dz} \right|_{z=h} = 0 \quad (13)$$

It may be expected that these conditions coincide, i.e., there can be no downstream flow where there is no driving force (Wells & Dorrell, 2021); however reality is more complex (Dorrell et al, 2016). Flow depth also may evolve in time. Table 3 compares the height of the flow estimated, where possible, from time-average flow parameters (Figures 15 and 18) using the dynamic boundary conditions, Equations 11-13, at the centre point of the channel $y=300\text{mm}$ (Figure 10).

From Table 3 it is concluded that there is no good consistent representation of flow height. However, the use of zero shear-stress condition does highlight that flows shallow as they are pushed towards the outer bank by positive Coriolis forces (Figure 17). Further, for negative Coriolis forces, as the flow is more uniformly distributed across the channel, flow depth also shallows as the flow is more evenly distributed across the channel (Figure 17).

The range in flow depth, and the complexity in deriving them means that any interpretation must be made with care. For this reason, here depth average flow velocity parameters are not explicitly determined.

5.2 Coriolis Controls on Flow Dynamics

As discussed in Section 2.2.1, turbidity currents run out for 100-1000's of kilometres via a process called auto-suspension (Parker et al, 1986; Wells & Dorrell, 2021). However, our understanding of autosuspension is limited: models predict energy is rapidly used up by the entrainment of ambient fluid, e.g., "flow mixing", prohibiting flow runout. Given the importance of ambient fluid entrainment on turbidity current dynamics and the known control of Coriolis forces on flow dynamics (Akhmetzhanov et al, 2007; Hesse et al, 1987), a key question is do Coriolis enhance or limit mixing and thus entrainment of ambient fluid.

The higher rotation rate in anticlockwise direction drags flow to the left hand-side (inner bend) of the channel and overcomes the centrifugal force which drags flow to the right hand-side (outer bend) (Figures 17-c, e, g, i). The tilt of zero-gradient (white line) is not as obvious as in the case of positive Rossby numbers (Figures 17-b, d, f, h), because Coriolis force and centrifugal force works against each other when it rotates anticlockwise. Eventually, the Coriolis force overcome the centrifugal force, which results in higher elevation at the inner bend of the channel if the rotation is fast enough.

A useful parameter to quantitatively describe mixing in stratified shear flow, such as turbidity currents, is the gradient Richardson number, Ri_g , Equation (6). The gradient Richardson number indicates the stability of the stratification of the flow (Kneller & Buckee, 2000), when Ri_g is less than $\frac{1}{4}$, stratification insufficient to limit flow instability, i.e. dampen turbulence (Turner, 1979). Turbulent instabilities are the major form of entrainment for density currents. Here results have been integrated to show velocity, density and gradient Richardson number profiles for clockwise rotating (Figures 18-b, d, f, h) and anticlockwise rotating (Figures 18-c, e, g, i) flow.

For all cases calculated Ri_g (Equation (6)) tends to go infinite at the height of velocity maximum because the velocity gradient is zero at this height. This may imply relatively stable flow in the centre of the current. However, the stability of this region, due to advection of turbulence, and the unsteady nature of real world flows has been the subject of some recent debate (Dorrell et al, 2018; Dorrell et al, 2019; Wells & Dorrell, 2021). Here, however, the mixing dynamics in the upper shear layer above the flow velocity maximum is of most interest, as mixing in this region determines entrainment of ambient fluid.

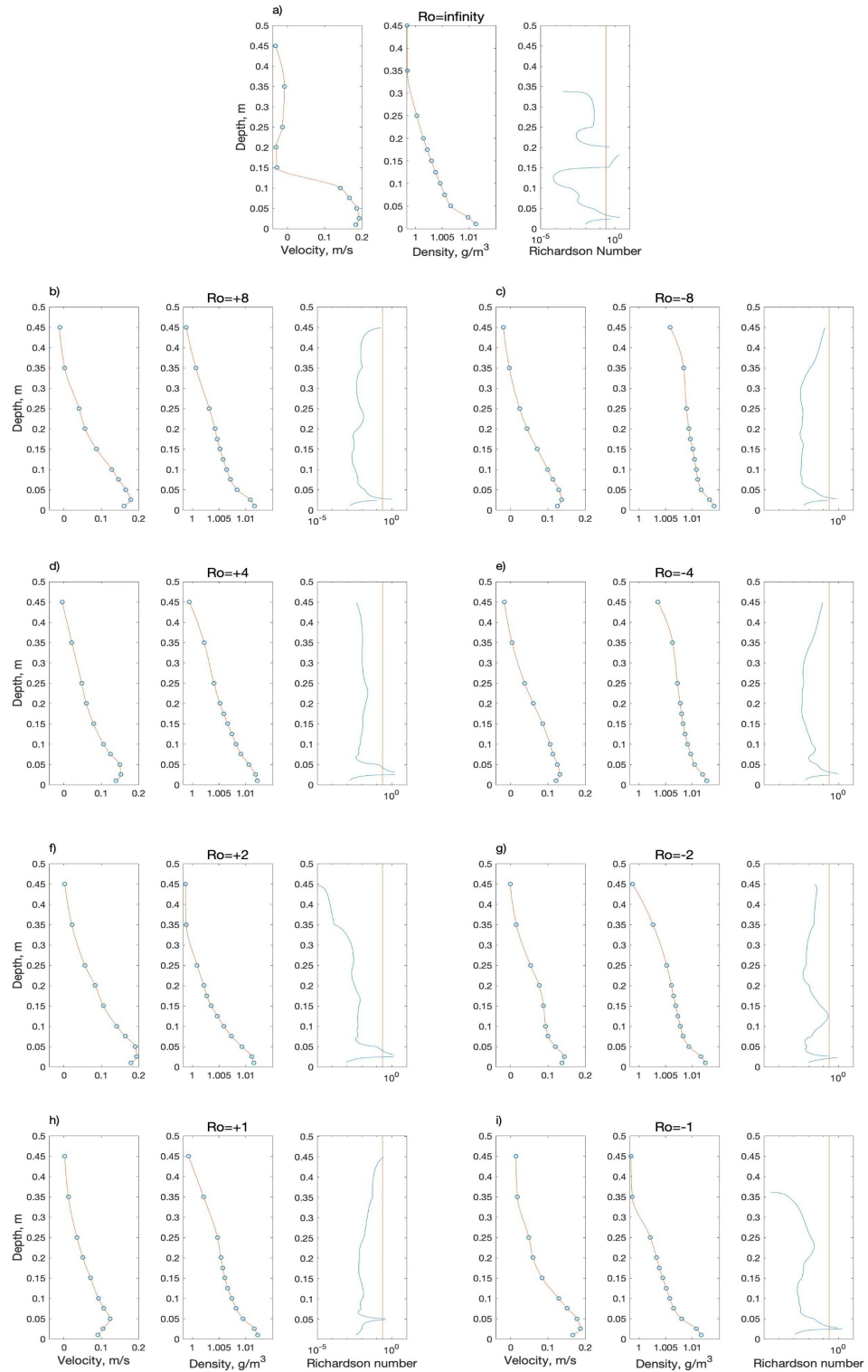


Figure 18 : Downstream velocity, density and gradient Richardson number (Equation (6)) profiles of gravity current at the second apex of the channel under different rotation rates ($Ro = \infty, \pm 8, \pm 4, \pm 2, \pm 1, =$). a) Flow in a non-rotational frame of reference, where the Rossby number ($Ro=U/Lf$) equals infinity. b), d), f) and h) Flow in a rotating frame of reference, subject to increasing pseudo Coriolis force towards the outer bank at Rossby numbers, b) $Ro=+8$, d) $Ro=+4$, f) $Ro=+2$, and h) $Ro=+1$. c), e), g) and i) Flow in a rotating frame of reference, subject to increasing pseudo Coriolis force towards the inner bank at Rossby numbers, c) $Ro=-8$; e) $Ro=-4$, g) $Ro=-2$, and i) $Ro=-1$. The critical $Rig=0.25$ is denoted by a red line.

For the case of zero rotation (Figure 18a) Ri_g is reduced in the upper shear layer to 0.12, although it does increase to infinity due to a local minimum in flow velocity near the flow ambient interface. Aside from this artefact the reduction in Ri_g is greater than seen than in any rotating flow (Figures 18b-i). An initial hypothesis is thus that turbulent mixing, and thus ambient fluid entrainment, is greater without Coriolis forces than with it. Put another way, modification of secondary flow by Coriolis forces (Dorrell et al, 2013) may thus limit ambient fluid entrainment. Next, mixing with increasing Coriolis forcing, i.e., decreasing Rossby number, are discussed.

For the clockwise rotating cases, Coriolis forces act with centrifugal forces, pushing the flow towards the outer bank (Figure 17). With increasing Coriolis forces this is seen to increase cross channel hydrostatic pressure gradient, i.e., slope of the interface between flow and ambient fluid, and decrease the maximum magnitude of secondary flow (compare Figures 17b, d, f and h). However, flow velocity at the “zero-shear” flow depth increases (compare Figures 17b, d, f and h). With increasing height above the velocity maximum the gradient Richardson number decreases from 0.25. Towards the upper limits of flow measurements, at 0.45m height, Ri_g then increases for $Ro = +8$ and $+1$; in all other cases it continuously decreases. In the region above the velocity maximum there is no immediately obvious general trend in gradient Richardson number. However, the magnitude of Ri_g may be seen to increase from just below 10^{-2} to just above 10^{-2} when Ro decreases from $+8$ to $+1$. Estimates of Ri_g based on downstream flow velocity may decrease if momentum is transferred into enhanced cross stream flow.

Similar patterns are observed for negative Rossby numbers. With depth above the velocity maximum, the gradient Richardson number decreases. Yet it remains larger than in the case of no Coriolis forcing. Looking at the secondary flow it is seen that when Coriolis force oppose centrifugal force the cross-channel flow velocity is enhanced. As above, transfer of momentum in the upper shear layer of the flow may influence calculation of Ri_g , and thus mixing, based on downstream velocity alone.

Centrifugal force caused by flow around a fluvial (or underwater) meander bend pushes the flow towards the outer bank. This is countered by a hydrostatic pressure gradient towards the inner bank, forming the cross-stream water slope. It is well documented how a cross-stream water slope can be seen to generate asymmetry in the submarine channel levees constructed by, and constraining, turbidity currents on the seafloor (Peakall & Sumner, 2015). As detailed previously (Dorrell et al, 2013), and herein (Figure 17), centrifugal-hydrostatic pressure balance is modified by Coriolis forces. It has been documented how this can fundamentally change the seafloor

channel levee development, generating levee slope asymmetry between left and right turning bends (Cossu & Wells, 2013; Davarpanah Jazi et al, 2020).

Here it is further suggested that both positive and negative Coriolis forces may lead to local increase in Ri_g within the flow. Whilst the interplay of flow and mixing processes remains unclear from study, this hypothesis suggests reduced mixing, and entrainment with increasing Rossby number. With mixing linked to entrainment and flow runout and Rossby number linked to latitude, it may be speculated that, as well as levee asymmetry, high latitude turbidity currents may be able to propagate more easily (suffer less entrainment) than low latitude systems.

5.3 Experimental Anomalies

A consistent feature of the experimental results has been the lack of clear trends in the empirical data, especially downstream flow velocity and flow buoyancy. This is most clearly evidenced in Figure 12, plotting buoyancy evolution with time. It is clearly seen that the case $Ro = \infty$, +2 and -1 are very similar. In these cases, at the measurement point (apex of the second channel bend, Figure 10) the buoyancy field does not evolve in time. Naively this is what we would expect for a pseudo-steady flow, where the flow may evolve in space but given constant influx conditions (Section 3) should remain constant in space (i.e., after the head has passed). The other experimental runs do not have this pseudo steady behaviour. For the $Ro = \pm 8$, ± 4 , -2 and +1 the flow buoyancy field thickens in time at the spatially *fixed* measurement point. This behaviour is not easily explained. However, when reviewing the experimental programme, Table 2, it is noted that the 13m diameter master basin was drained and refilled with clean water before the start of $Ro = \infty$, +2 and -1 runs only. In these cases, the flow from the channel emptied into a purely freshwater basin.

In all experiments the basin was continuously drained to remove denser than ambient salt water and salinity of the ambient was monitored. However, in the runs where $Ro = \pm 8$, ± 4 , -2 and +1 the ambient in the basin was likely still “*polluted*” by the discharge from the previous runs. It is therefore postulated that the dynamics of the flows in these runs were directly affected by the different experimental setup. It is plausible that, when not fully drained, high density solution from previous experiments may have pooled at the end of the channel. Such high density solutions could have formed a blockage at the end of the channel, resulting in a high density saline wedge propagating up channel during the course of the experiment. An up channel

propagating saline wedge would explain the thickening of the buoyancy field over time, as observed in Figure 12.

Further to this downstream and cross-stream velocity measurements were made at different times, to avoid cross-talk between the UVP probes (Section 3). Cross stream flow velocity was sampled from 5-15 minutes, downstream flow velocity was measured from 25-35 minutes. With exception of the $Ro = \infty$, +2 and -1 cases, measurement timing means that:

- I. Flow depth, downstream and cross stream flow velocity measurements are not directly comparable.
- II. Late time measurements (i.e., downstream flow velocity) are likely most polluted by upstream propagating channel blockage and are thus least reliable.

In summary whilst tentative conclusions may be drawn from the results of these experiments, the experiments themselves may be subject to inherent bias that masks any underlying trend in flow dynamics.

Chapter 6 Conclusions

Here it has been discussed how the Coriolis force may have a significant impact on the dynamics of oceanic density driven flows, turbidity currents, in seafloor channels especially in sinuous channels. Submarine fans are the largest sedimentary deposits on the Earth surface. Seafloor channels are important as the conduits for sediment, nutrient and pollutant transport within the deep ocean.

It was reviewed how seafloor channel evolution is the outcome of the dynamic interaction between turbidity currents and the seafloor, as well as the forces acting on the flow. This study investigated the effect of Coriolis forces, inherent to real world flows due to Earth's rotation. However, modelling Coriolis forces in the lab is difficult, as by definition it requires a rotating frame of reference. It is even more complicated to scale Coriolis force with other key flow parameters, including the ratio of inertial to viscous forces, the Reynolds number, and inertial to gravitational forces the Froude number (or inverse Richardson number). For the first time the effect of experimentally scaled Coriolis force on mixing of turbulent flow is reported. Internal flow dynamics are measured at a bend apex, as analogous to real-world sinuous channel systems. An important impact identified is how ambient fluid is entrained, which is critical for understanding gravity current dynamics (Hacker et al, 1996). This had previously not been considered. Experiments quantified the downslope and cross slope velocity, as well as the density, for various rotating rates, across a range of Rossby numbers. It is speculated that enhanced secondary flow with increasing Coriolis force results in reduced mixing.

The detailed results of this study suggest the Coriolis force has a significant impact on the density structure, as well as the direction and intensity of internal flows inside a saline gravity current running down a deep-water channel. Under the influence of the Coriolis force, the direction of the bottom boundary layer of a gravity current and the location of the maximum velocity core alter, resulting in uneven right and left-turning bends. On the other hand, the denser fluid, always stays near the outer bend, creating a hydraulic mechanism for stabilizing bend evolution at higher latitudes. Strong Coriolis forces, in addition, can change the course of near-bed secondary flow, which is expected to have a significant impact on sediment load in turbidity currents and, as a result, the formation of sinuous and straight deep-water channels at various latitudes.

This work provides the most extensive density and velocity measurements of scale gravity current, with and without rotation, due to the utilization of a rotating 13 m radius channel. The size of facility enabled study of both scaled Rossby number and unprecedented high Reynolds number flows. These observations are the largest and most turbulent gravity currents investigated under the action of Coriolis force, providing a bridge to field-scale gravity currents. However, the experimental methodology was robustly critiqued. Failure to drain the master basin between experiments may have resulted in previous experiments “*polluting*” the empirical data. It is concluded that further work is required to test the robustness of the methodology used and the conclusions drawn from the research. Further, key topics for future research within the field are highlighted, including scaling of Reynolds number and sediment transport, the impact of channel aspect ratio and the effect of downslope gradient and gravitational force. These important considerations are left as hypothesis for future work.

6.1 Future work

Section 5.3 details plausible explanation for some of the anomalous behaviour of experiments conducted. A potential major criticism of the experimental campaign was that the master basin was only refreshed three times, before the $Ro = \infty$, +2 and -1 experiments. This represented a trade-off between access time to the experimental facility and need to study a parameter space of flow dynamics. Ultimately future work will need to be conducted, repeating the work conducted, testing the effect of draining the master basin on flow dynamics and thus advancing experimental methodology. This could be done using small scale facilities (Cossu & Wells, 2013) before going back to large scale facilities (Davaranah Jazi et al, 2020) where turbulent flow can be resolved. That this issue has been identified is an important finding in advancing methodology used in experimental fluid dynamics.

Further to the potential limitations of the experimental methodology, the experiments themselves only touched the surface of the wide range of potential leading order control parameters on gravity current flow dynamics. Limiting study to channelised gravity currents, subject to Coriolis forces, analogous to many turbidity current systems a range of other parameters is reviewed as in need of future study. Firstly, experimental research on the Coriolis force's impact on these channels' flow dynamics has been restricted to relatively low Reynolds numbers and data collection has been limited to velocity profiles and isolated low-resolution two-dimensional cross-sectional velocity fields (Cenedese & Adduce, 2008; Cenedese et al, 2004; Cossu & Wells, 2013; Cossu et al, 2010). Secondly experiments, including those presented herein,

have only been carried out over a narrow range of channel sizes, width: depth, or aspect ratios, rotation rates (Coriolis parameter f from -1 to $+1 \text{ s}^{-1}$) and slopes (0.02-0.7).

The relatively low Reynolds number of previous scale experiments means that turbulence is likely a poor representation of real-world systems, as at low Reynolds number experimental flows may be subject to local re-laminarization from energy sink into buoyancy production (Caulfield, 2021). This transitional nature of turbulence means that flow mixing, and thus ambient fluid entrainment is likely poorly described. Further, weak turbulent mixing prohibits the turbulent suspension of sediment, as in real-world turbidity currents. This has meant that many experiments have relied on the use of saline solution, as herein, as a proxy for sediment-laden flow. This has the disadvantage of failing to describe work done against keeping sediment in suspension, or the work gained from sediment erosion (Luchi et al, 2018). In general, future experiments on turbidity currents are likely needed at larger scale, or an appropriate scaling of dilute (Simmons et al, 2020) sediment transport needs to be developed.

Parker (1976) suggest that braided planform development in subaerial systems is essentially a response to flow instability, which is controlled by the depth-width (aspect) ratio of the flow. Assuming submarine channels have some similarity to rivers, channel aspect ratio therefore may be a key parameter controlling morphodynamics. Indeed experiments conducted by Foreman et al (2015) combined with other field observations and experimental tests suggested that the aspect ratio of the density currents determine the planar morphology of the submarine channels. Further, Kane et al (2008) conducted experiments directly on aspect ratio (width divided by height) effect on a seafloor channel bend. The aspect ratio was varied between 4 and 25. It was seen that depositional focus from the outer bend in an aspect ratio of a 25 aspect ratio channel shifted to the inner bend in the 4 aspect ratio channel. This is important as it suggests that channels reach a quasi-steady planform geometry as maintained by deposition at the inner bend by frequent equilibrium currents, and deposition at the outer bend by larger, less frequent, disequilibrium currents. By changing aspect-ratio, the morphology of submarine channels will be impacted. However, to-date there has been no work considering how change in aspect ratio affects the impact of Coriolis force on gravity current dynamics. It is hypothesised that with at greater aspect ratios the effect of the flow ambient interface slope will be increasingly important. In wide enough channels the flow may ultimately detach itself from a side wall confinement. This loss of confinement would result in a new interface between flow and ambient flow developing, increasing ambient fluid entrainment and flow drag. However, this hypothesis is left here for consideration of future work.

Finally, previous studies have argued that there is a strong dependence of entrainment parameter on the slope angle (Cenedese & Adduce, 2008; Cenedese et al, 2004; Ellison & Turner, 1959; Özgökmen & Chassignet, 2002). Experiments and numerical modelling showed that the entrainment coefficient increases with increasing slope angles. (Özgökmen & Chassignet, 2002), and this can be explained by the fact that as the angle of inclination increases, increases the gravitational force, driving faster flow, creating greater shear and causing larger entrainment (Özgökmen & Chassignet, 2002). Cenedese et al (2004) conducted experiments found that when the slope and the density of bottom currents increase, the flow regime evolves from laminar to turbulent. The mixing efficiency also increases when passing through the laminar to wave regime. Studies conducted so far have not reviewed the co-dependence of mixing and entrainment, Coriolis force and slope. It is hypothesised that mixing will increase with increased slope but may be limited by Coriolis force. This is left to future work to consider.

References

- Abad, J. D., Sequeiros, O. E., Spinewine, B., Pirmez, C., Garcia, M. H. & Parker, G. (2011) Secondary current of saline underflow in a highly meandering channel: experiments and theory. *Journal of Sedimentary Research*, 81(11), 787-813.
- Acheson, D. J. (1990) *Elementary fluid dynamics*. Oxford: Oxford University Press.
- Akhmetzhanov, A., Kenyon, N., Habgood, E., Van Der Mollen, A., Nielsen, T., Ivanov, M. & Shashkin, P. (2007) North Atlantic contourite sand channels. *Geological Society, London, Special Publications*, 276(1), 25-47.
- Altinakar, M., Graf, W. & Hopfinger, E. (1996) Flow structure in turbidity currents. *Journal of Hydraulic Research*, 34(5), 713-718.
- American Heritage® Dictionary of the English Language, F. E. (2023) *pseudo force*, 2023. Available online: <https://www.thefreedictionary.com/pseudo+force> [Accessed].
- Amy, L., Peakall, J. & Talling, P. (2005) Density-and viscosity-stratified gravity currents: Insight from laboratory experiments and implications for submarine flow deposits, 179(1-2), 5-29.
- Arnol'd, V. I. (2013) *Mathematical methods of classical mechanics*, 60. New York: Springer Science & Business Media.
- Ashford, O. M. (1985) *Prophet or professor?: the life and work of Lewis Fry Richardson*. Bristol, UK: Adam Hilger Ltd.
- Azpiroz-Zabala, M., Cartigny, M. J., Talling, P. J., Parsons, D. R., Sumner, E. J., Clare, M. A., Simmons, S. M., Cooper, C. & Pope, E. L. (2017) Newly recognized turbidity current structure can explain prolonged flushing of submarine canyons. *Science Advances*, 3(10), e1700200.
- Azpiroz-Zabala, M., Cartigny, M. J., Sumner, E. J., Clare, M., Talling, P. J., Parsons, D. R. & Cooper, C. (2017) A general model for the helical structure of geophysical flows in channel bends, 44(23).
- Baines, P. G. (1998) *Topographic effects in stratified flows*. Cambridge: Cambridge University Press.
- Banerjee, P. K. (2004) *Oceanography for beginners*. Mumbai, India: Allied Publishers Pvt. Ltd.
- Barry, R. G. C., Richard J (2009) *Atmosphere, weather and climate*. Oxon: Routledge.
- Batchelor, G. (1967) An introduction to fluid dynamics. *Cambridge: UP xviii*, 615.
- Benjamin, T. B. (1968) Gravity currents and related phenomena. *Journal of Fluid Mechanics*, 31(2), 209-248.

- Best, J. L., Kostaschuk, R. A., Peakall, J., Villard, P. V. & Franklin, M. (2005) Whole flow field dynamics and velocity pulsing within natural sediment-laden underflows. *Geology*, 33(10).
- Bhatia, V. B. (1997) *Classical mechanics: With introduction to nonlinear oscillations and chaos* Alpha Science Int'l Ltd.
- Birman, V. K. M., E; Kneller, B (2009) The shape of submarine levees: exponential or power law?, 619, 367-376.
- Boubnov, B. & Golitsyn, G. S. (1995) *Convection in rotating fluids*. Berlin: Springer.
- Boussinesq, J. (1897) *Théorie de l'écoulement tourbillonnant et tumultueux des liquides dans les lits rectilignes à grande section*, 1Gauthier-Villars.
- Bowen, A. J., Normark, W. R. & Piper, D. J. (1984) Modelling of turbidity currents on Navy submarine fan, California continental borderland. *Sedimentology*, 31(2), 169-185.
- Bowker, K. (1988) Albert Einstein and meandering rivers, 7(1), 45-45.
- Buckee, C., Kneller, B. & Peakall, J. (2001) Turbulence structure in steady, solute-driven gravity currents, *Particulate gravity currents* International Association of Sedimentologists, Special Publication 31, 173-188.
- Caulfield, C. P. (2021) Layering, Instabilities, and Mixing in Turbulent Stratified Flows. *Annual Review of Fluid Mechanics*, 53(1), 113-145.
- Cenedese, C. & Adduce, C. (2008) Mixing in a density-driven current flowing down a slope in a rotating fluid. *Journal of Fluid Mechanics*, 604, 369-388.
- Cenedese, C., Whitehead, J. A., Ascarelli, T. & Ohiwa, M. (2004) A dense current flowing down a sloping bottom in a rotating fluid. *Journal of Physical Oceanography*, 34(1), 188-203.
- Corney, R. K., Peakall, J., Parsons, D. R., Elliott, L., Amos, K. J., Best, J. L., Keevil, G. M. & Ingham, D. B. (2006) The orientation of helical flow in curved channels. *Sedimentology*, 53(2), 249-257.
- Cossu, R., Forrest, A. L., Roop, H. A., Dunbar, G. B., Vandergoes, M. J., Levy, R. H., Stumpner, P. & Schladow, S. G. (2016) Seasonal variability in turbidity currents in Lake Ohau, New Zealand, and their influence on sedimentation. *Marine and Freshwater Research*, 67(11).
- Cossu, R. & Wells, M. G. (2010) Coriolis forces influence the secondary circulation of gravity currents flowing in large-scale sinuous submarine channel systems. *Geophysical Research Letters*, 37.
- Cossu, R. & Wells, M. G. (2013) The evolution of submarine channels under the influence of Coriolis forces: experimental observations of flow structures. *Terra Nova*, 25(1), 65-71.

Cossu, R., Wells, M. G. & Wahlin, A. K. (2010) Influence of the Coriolis force on the velocity structure of gravity currents in straight submarine channel systems. *Journal of Geophysical Research-Oceans*, 115.

Cossu, R. a. W., M. G. (2012) A comparison of the shear stress distribution in the bottom boundary layer of experimental density and turbidity currents. *European Journal of Mechanics B-Fluids*, 32, 70-79.

Davarpanah Jazi, S., Wells, M. G., Peakall, J., Dorrell, R. M., Thomas, R. E., Keevil, G. M., Darby, S. E., Sommeria, J., Viboud, S. & Valran, T. (2020) Influence of Coriolis Force Upon Bottom Boundary Layers in a Large-Scale Gravity Current Experiment: Implications for Evolution of Sinuous Deep-Water Channel Systems. *Journal of Geophysical Research: Oceans*, 125(3).

De Leeuw, J. E., Joris T; Cartigny, Matthieu JB (2016) Morphodynamics of submarine channel inception revealed by new experimental approach. *Nature communications*, 7, 10886.

Dietrich, W. E. & Smith, J. D. (1983) Influence of the point bar on flow through curved channels. *Water Resources Research*, 19(5), 1173-1192.

Dorrell, R., Amy, L., Peakall, J. & McCaffrey, W. (2018) Particle size distribution controls the threshold between net sediment erosion and deposition in suspended load dominated flows. *Geophysical Research Letters*, 45(3), 1443-1452.

Dorrell, R., Darby, S., Peakall, J., Sumner, E., Parsons, D. & Wynn, R. (2013) Superelevation and overspill control secondary flow dynamics in submarine channels. *Journal of Geophysical Research: Oceans*, 118(8), 3895-3915.

Dorrell, R., Darby, S., Peakall, J., Sumner, E., Parsons, D. & Wynn, R. (2014) The critical role of stratification in submarine channels: Implications for channelization and long runout of flows. *Journal of Geophysical Research: Oceans*, 119(4), 2620-2641.

Dorrell, R., Peakall, J., Sumner, E., Parsons, D., Darby, S., Wynn, R., Özsoy, E. & Tezcan, D. (2016) Flow dynamics and mixing processes in hydraulic jump arrays: Implications for channel-lobe transition zones. *Marine Geology*, 381, 181-193.

Dorrell, R. M., Peakall, J., Darby, S. E., Parsons, D. R., Johnson, J., Sumner, E. J., Wynn, R. B., Ozsoy, E. & Tezcan, D. (2019) Self-sharpening induces jet-like structure in seafloor gravity currents. *Nat Commun*, 10(1), 1381.

Ekman, V. W. (1905) On the influence of the earth's rotation on ocean-currents. *Arkiv for Matematik, Astronomi och Fysik*, 2, 1-52.

Ellison, T. & Turner, J. (1959) Turbulent entrainment in stratified flows. *Journal of Fluid Mechanics*, 6(3), 423-448.

Ezz, H. & Imran, J. (2014) Curvature-induced secondary flow in submarine channels, 14(2), 343-370.

- Faller, A. J. (1963) An experimental study of the instability of the laminar Ekman boundary layer. *Journal of Fluid Mechanics*, 15(4), 560-576.
- Ferguson, R. I., Parsons, D. R., Lane, S. N. & Hardy, R. J. (2003) Flow in meander bends with recirculation at the inner bank. *Water Resources Research*, 39(11).
- Feynman, R. P., Leighton, R. B. & Sands, M. (1965) The feynman lectures on physics; vol. i. *American Journal of Physics*, 33(9), 750-752.
- Foreman, B. Z., Lai, S. Y., Komatsu, Y. & Paola, C. (2015) Braiding of submarine channels controlled by aspect ratio similar to rivers. *Nature Geoscience*, 8(9), 700.
- Garcia, M. & Parker, G. (1993) Experiments on the entrainment of sediment into suspension by a dense bottom current. *Journal of Geophysical Research: Oceans*, 98(C3), 4793-4807.
- Garcia, M. H. (1994) Depositional turbidity currents laden with poorly sorted sediment. *Journal of Hydraulic Engineering*, 120(11), 1240-1263.
- Gregory, N. & Walker, W. (1960) Experiments on the effect of suction on the flow due to a rotating disk. *Journal of Fluid Mechanics*, 9(2), 225-234.
- Griffiths, R. & Linden, P. (1982) Laboratory experiments on fronts: Part I: Density-driven boundary currents, 19(3-4), 159-187.
- Hacker, J., Linden, P. & Dalziel, S. (1996) Mixing in lock-release gravity currents. *Dynamics of Atmospheres and Oceans*, 24(1-4), 183-195.
- Hage, S., Cartigny, M. J., Clare, M. A., Sumner, E. J., Vendettuoli, D., Hughes Clarke, J. E., Hubbard, S. M., Talling, P. J., Lintern, D. G. & Stacey, C. D. (2018) How to recognize crescentic bedforms formed by supercritical turbidity currents in the geologic record: Insights from active submarine channels. *Geology*, 46(6), 563-566.
- Hesse, R., Chough, S. K. & Rakofsky, A. (1987) The Northwest Atlantic mid-ocean channel of the Labrador sea. V. Sedimentology of a giant deep-sea channel. *Canadian Journal of Earth Sciences*, 24(8), 1595-1624.
- Imran, J., Islam, M. A., Huang, H., Kassem, A., Dickerson, J., Pirmez, C. & Parker, G. (2007) Helical flow couplets in submarine gravity underflows. *Geology*, 35(7), 659-662.
- Islam, M. A. & Imran, J. (2008) Experimental modeling of gravity underflow in a sinuous submerged channel. *Journal of Geophysical Research: Oceans*, 113(C7).
- Islam, M. A. & Imran, J. (2010) Vertical structure of continuous release saline and turbidity currents. *Journal of Geophysical Research Oceans*, 115(C8), 396-413.

- Ivanov, V., Shapiro, G., Huthnance, J., Aleynik, D. & Golovin, P. (2004) Cascades of dense water around the world ocean. *Progress in oceanography*, 60(1), 47-98.
- Kane, I. A., McCaffrey, W. D. & Peakall, J. (2008) Controls on sinuosity evolution within submarine channels. *Geology*, 36(4), 287-290.
- Kassem, A. & Imran, J. (2004) Three-dimensional modeling of density current. II. Flow in sinuous confined and unconfined channels. *Journal of Hydraulic Research*, 42(6), 591-602.
- Keevil, G. M., Peakall, J., Best, J. L. & Amos, K. J. (2006) Flow structure in sinuous submarine channels: velocity and turbulence structure of an experimental submarine channel, 229(3-4), 241-257.
- Kelly, R., Dorrell, R., Burns, A. & McCaffrey, W. (2019) The structure and entrainment characteristics of partially-confined gravity currents.
- Kelly, R. W. (2018) *Seafloor gravity currents: flow dynamics in overspilling and sinuous channels* University of Leeds.
- Klaucke, I., Hesse, R. & Ryan, W. B. (1998) Morphology and structure of a distal submarine trunk channel: The Northwest Atlantic Mid-Ocean Channel between lat 53 N and 44 30' N. *Geological Society of America Bulletin* 110(1), 22-34.
- Kneller, B. & Buckee, C. (2000) The structure and fluid mechanics of turbidity currents: a review of some recent studies and their geological implications. *Sedimentology*, 47, 62-94.
- Kneller, B. C., Bennett, S. J. & McCaffrey, W. D. (1997) Velocity and turbulence structure of density currents and internal solitary waves: potential sediment transport and the formation of wave ripples in deep water. *Sedimentary Geology*, 112(3-4), 235-250.
- Kneller, B. C., Bennett, S. J. & McCaffrey, W. D. (1999) Velocity structure, turbulence and fluid stresses in experimental gravity currents. *Journal of Geophysical Research-Oceans*, 104, 5381-5391.
- Kolla, V., Bourges, P., Urruty, J.-M. & Safa, P. (2001) Evolution of deep- water Tertiary sinuous channels offshore Angola (west Africa) and implications for reservoir architecture. *AAPG Bulletin*, 85, 1373-1405.
- Kolla, V., Posamentier, H. W. & Wood, L. J. (2007) Deep-water and fluvial sinuous channels—Characteristics, similarities and dissimilarities, and modes of formation. *Marine and Petroleum Geology*, 24(6-9), 388-405.
- Langbein, W. B. & Leopold, L. B. (1970) River meanders and the theory of minimum variance, *Rivers and river terraces*. London: Springer, 238-263.

- Legg, S., Briegleb, B., Chang, Y., Chassignet, E. P., Danabasoglu, G., Ezer, T., Gordon, A. L., Griffies, S., Hallberg, R. & Jackson, L. (2009) Improving oceanic overflow representation in climate models: the gravity current entrainment climate process team. *Bulletin of the American Meteorological Society*, 90(5), 657-670.
- Lonsdale, P. & Hollister, C. D. (1979) Cut-off at an abyssal meander south of Iceland. *Geology*, 7, 597-601.
- Lowe, R. J., Linden, P. & Rottman, J. W. (2002) A laboratory study of the velocity structure in an intrusive gravity current. *Journal of Fluid Mechanics*, 456, 33-48.
- Luchi, R., Balachandar, S., Seminara, G. & Parker, G. (2018) Turbidity Currents With Equilibrium Basal Driving Layers: A Mechanism for Long Runout. *Geophysical Research Letters*, 45(3), 1518-1526.
- Marshall, C. R., Dorrell, R. M., Dutta, S., Keevil, G. M., Peakall, J. & Tobias, S. M. (2021a) The effect of Schmidt number on gravity current flows: The formation of large-scale three-dimensional structures. *Physics of Fluids*, 33(10).
- Marshall, C. R., Dorrell, R. M., Keevil, G. M., Peakall, J. & Tobias, S. M. (2021b) Observations of large-scale coherent structures in gravity currents: implications for flow dynamics. *Experiments in Fluids*, 62(6).
- Maslin, M., Knutz, P. C. & Ramsay, T. (2006) Millennial-scale sea-level control on avulsion events on the Amazon Fan. *Quaternary Science Reviews*, 25(23-24), 3338-3345.
- Meiburg, E. & Kneller, B. (2010) Turbidity currents and their deposits. *Annual Review of Fluid Mechanics*, 42, 135-156.
- Middleton, G. (1969) *The New Concepts of Continental Margin Sedimentation*. AGI Short Course Lecture Notes.
- Middleton, G. V. (1966a) Experiments on density and turbidity currents: I. Motion of the head. *Canadian Journal of Earth Sciences*, 3(4), 523-546.
- Middleton, G. V. (1966b) EXPERIMENTS ON DENSITY AND TURBIDITY CURRENTS: II. UNIFORM FLOW OF DENSITY CURRENTS. *Canadian Journal of Earth Sciences*, 3(5), 10.
- Middleton, G. V. (1993) Sediment Deposition from Turbidity Currents. *Annual Review of Earth and Planetary Sciences*, 21, 89-114.
- Middleton, G. V. & Hampton, M. A. (1973) Part I. Sediment gravity flows: mechanics of flow and deposition. *Geology*.
- Mountjoy, J. J., Howarth, J. D., Orpin, A. R., Barnes, P. M., Bowden, D. A., Rowden, A. A., Schimel, A. C. G., Holden, C., Horgan, H. J., Nodder, S. D., Patton, J. R., Lamarche, G., Gerstenberger, M.,

- Micallef, A., Pallentin, A. & Kane, T. (2018) Earthquakes drive large-scale submarine canyon. *Science Advances*, 4 (3), eaar3748.
- Mulder, T., Savoye, B. & Syvitski, J. (1997) Numerical modelling of a mid-sized gravity flow: the 1979 Nice turbidity current (dynamics, processes, sediment budget and seafloor impact). *Sedimentology*, 44(2), 305-326.
- Mulder, T., Syvitski, J. P. M., Migeon, S., Faugères, J.-C. & Savoye, B. (2003) Marine hyperpycnal flows: initiation, behavior and related deposits. A review. *Marine and Petroleum Geology*, 20(6-8), 861-882.
- Munson, B. R., Okiishi, T. H., Huebsch, W. W. & Rothmayer, A. P. (2013) *Fluid mechanics*. Hoboken, NJ: John Wiley & Sons, Inc.
- Nakajima, T. & Kneller, B. (2013) Quantitative analysis of the geometry of submarine external levees, 60(4), 877-910.
- Nittrouer, C. A. & Wright, L. D. (1994) Transport of particles across continental shelves. *Reviews of Geophysics*, 32(1), 85-113.
- Nogueira, H. I. A., Claudia; Alves, Elsa; Franca, Mário J (2014) Dynamics of the head of gravity currents. *Environmental Fluid Mechanics*, 14(2), 519-540.
- Normark, W. R. (1989) Observed parameters for turbidity-current flow in channels, Reserve Fan, Lake Superior. *Journal of Sedimentary Research*, 59(3), 423-431.
- Özgökmen, T. M. & Chassignet, E. P. (2002) Dynamics of two-dimensional turbulent bottom gravity currents. *Journal of Physical Oceanography*, 32(5), 1460-1478.
- Paola, C., Straub, K., Mohrig, D. & Reinhardt, L. (2009) The “unreasonable effectiveness” of stratigraphic and geomorphic experiments. *Earth-Science Reviews*, 97(1-4), 1-43.
- Parker, G. (1976) On the cause and characteristic scales of meandering and braiding in rivers. *Journal of fluid mechanics*, 76(3), 457-480.
- Parker, G., Fukushima, Y. & Pantin, H. M. (1986) Self-accelerating turbidity currents. *Journal of Fluid Mechanics*, 171, 145-181.
- Parsons, D. R., Peakall, J., Aksu, A. E., Flood, R. D., Hiscott, R. N., Beşiktepe, Ş. & Moulard, D. (2010) Gravity-driven flow in a submarine channel bend: Direct field evidence of helical flow reversal. *Geology*, 38(12), 1063-1066.
- Parsons, J. D., Friedrichs, C. T., Traykovski, P. A., Mohrig, D., Imran, J., Syvitski, J. P. M., Parker, G., Puig, P., Buttles, J. L. & Garcia, M. H. o. (2007) The mechanics of marine sediment gravity flows. *Continental Margin Sedimentation: From Sediment Transport to Sequence Stratigraphy*, 275-333.

- Paull, C. K., Talling, P. J., Maier, K. L., Parsons, D., Xu, J., Caress, D. W., Gwiazda, R., Lundsten, E. M., Anderson, K. & Barry, J. P. (2018) Powerful turbidity currents driven by dense basal layers. *Nature Communications*, 9(1), 4114.
- Peakall, J., Felix, M., McCaffrey, B. & Kneller, B. (2001) Particulate gravity currents: Perspectives. *Particulate Gravity Currents*, 16, 1-8.
- Peakall, J., Kane, I. A., Masson, D. G., Keevil, G., McCaffrey, W. & Corney, R. (2012) Global (latitudinal) variation in submarine channel sinuosity. *Geology*, 40(1), 11-14.
- Peakall, J., McCaffrey, B. & Kneller, B. (2000) A process model for the evolution, morphology, and architecture of sinuous submarine channels, 70(3), 434-448.
- Peakall, J. & Sumner, E. J. (2015) Submarine channel flow processes and deposits: A process-product perspective. *Geomorphology*, 244, 95-120.
- Pedlosky, J. (1987) *Geophysical fluid dynamics 2nd edition*, 710. New York, NY: Springer.
- Peltier, W. R. & Caulfield, C. P. (2003) Mixing Efficiency in Stratified Shear Flows. *Annual Review of Fluid Mechanics*, 35(1), 135-167.
- Persson, A. (1998) How do we understand the Coriolis force? *Bulletin of the American Meteorological Society*, 79(7), 1373-1386.
- Piper, D. J. & Deptuck, M. (1997) Fined-grained turbidites of the Amazon Fan: facies characterization and interpretation. *Integrated Ocean Drilling Program: Preliminary Reports*, 155, 79-108.
- Pirmez, C. (1994) *Growth of a submarine meandering channel-levee system on the Amazon Fan* Columbia University.
- Pirmez, C. & Imran, J. (2003) Reconstruction of turbidity currents in Amazon Channel. *Marine and petroleum geology*, 20(6-8), 823-849.
- Price, M. B. A. W. A. (1994) *Coastal, Estuarial, and Harbour Engineers' Reference Book* Taylor & Francis.
- Ravenne, C. & Beghin, P. (1983) Apport des expériences en canal à l'interprétation sédimentologique des dépôts de cônes détritiques sous-marins. *Revue de l'Institut Français du Pétrole*, 38(3), 279-297.
- Reynolds, O. (1883) An experimental investigation of the circumstances which determine whether the motion of water shall be direct or sinuous. *Royal Society*, 24, 935.
- Rozovskii, I. L. (1957) *Flow of water in bends of open channels*. Kiev: Academy of Sciences of the Ukrainian SSR.

- Sequeiros, O. E., Spinewine, B., Beaubouef, R. T., Sun, T., García, M. H. & Parker, G. (2010) Characteristics of velocity and excess density profiles of saline underflows and turbidity currents flowing over a mobile bed. *Journal of Hydraulic Engineering*, 136(7), 412-433.
- Simmons, S. M., Azpiroz-Zabala, M., Cartigny, M. J. B., Clare, M. A., Cooper, C., Parsons, D. R., Pope, E. L., Sumner, E. J. & Talling, P. J. (2020) Novel Acoustic Method Provides First Detailed Measurements of Sediment Concentration Structure Within Submarine Turbidity Currents. *Journal of Geophysical Research: Oceans*, 125(5).
- Simpson, J. & Britter, R. (1979) The dynamics of the head of a gravity current advancing over a horizontal surface, 94(3), 477-495.
- Simpson, J. E. (1972) Effects of the lower boundary on the head of a gravity current, 53(4), 759-768.
- Simpson, J. E. (1982) Gravity currents in the laboratory, atmosphere, and ocean. *Annual Review of Fluid Mechanics*, 14(1), 213-234.
- Simpson, J. E. (1986) Mixing at the Front of a Gravity Current. *Acta Mechanica*, 63(1-4), 245-253.
- Simpson, J. E. (1999) *Gravity currents: In the environment and the laboratory*. UK: Cambridge university press.
- Smit, R. & Kaeser, A. (2016) Defining freshwater mussel mesohabitat associations in an alluvial, Coastal Plain river. *Freshwater Science*, 35(4), 1276-1290.
- Stacey, M. W. & Bowen, A. J. (1988) The Vertical Structure of Density and Turbidity Currents - Theory and Observations. *Journal of Geophysical Research-Oceans*, 93(C4), 3528-3542.
- Stagnaro, M. & Bolla Pittaluga, M. (2014) Velocity and concentration profiles of saline and turbidity currents flowing in a straight channel under quasi-uniform conditions. *Earth Surface Dynamics*, 2(1), 167-180.
- Stevenson, C. J., Talling, P. J., Masson, D. G., Sumner, E. J., Frenz, M. & Wynn, R. B. (2014) The spatial and temporal distribution of grain-size breaks in turbidites. *Sedimentology*, 61(4), 1120-1156.
- Straub, K. M. & Mohrig, D. (2008) Quantifying the morphology and growth of levees in aggrading submarine channels, 113(F3).
- Straub, K. M., Mohrig, D., McElroy, B., Buttles, J. & Pirmez, C. (2008) Interactions between turbidity currents and topography in aggrading sinuous submarine channels: A laboratory study. *Geological Society of America Bulletin*, 120(3-4), 368-385.
- Stuart, J. (1954) On the effects of uniform suction on the steady flow due to a rotating disk. *The Quarterly Journal of Mechanics and Applied Mathematics*, 7(4), 446-457.

Sumner, E., Peakall, J., Dorrell, R., Parsons, D., Darby, S., Wynn, R., McPhail, S., Perrett, J., Webb, A. & White, D. (2014) Driven around the bend: Spatial evolution and controls on the orientation of helical bend flow in a natural submarine gravity current. *Journal of Geophysical Research: Oceans*, 119(2), 898-913.

Sumner, E., Peakall, J., Parsons, D., Wynn, R., Darby, S., Dorrell, R., McPhail, S., Perrett, J., Webb, A. & White, D. (2013) First direct measurements of hydraulic jumps in an active submarine density current. *Geophysical Research Letters*, 40(22), 5904-5908.

Talley, L. D. (2011) *Descriptive physical oceanography: an introduction*. Boston Academic press.

Talling, P. J., Allin, J., Armitage, D. A., Arnott, R. W., Cartigny, M. J., Clare, M. A., Felletti, F., Covault, J. A., Girardclos, S. & Hansen, E. (2015) Key Future Directions For Research On Turbidity Currents and Their Deposits. *Journal of Sedimentary Research*, 85(2), 153-169.

Tesaker, E. (1969) Uniform turbidity currents. *Unpublished doctoral thesis, Technical University of Norway, Trondheim*.

Tritton, D. J. (2012) *Physical fluid dynamics*. Berkshire, UK: Springer Science & Business Media.

Turner, J. S. (1979) *Buoyancy effects in fluids*. Cambridge, UK: Cambridge University Press.

Vallis, G. K. (2016) Geophysical fluid dynamics: whence, whither and why? *The Royal Society*, 472(2192), 20160140.

Wåhlin, A. (2004) Downward channeling of dense water in topographic corrugations. *Deep Sea Research Part I: Oceanographic Research Papers*, 51(4), 577-590.

Wåhlin, A., Darelius, E., Cenedese, C. & Lane-Serff, G. (2008) Laboratory observations of enhanced entrainment in dense overflows in the presence of submarine canyons and ridges. *Deep Sea Research Part I: Oceanographic Research Papers*, 55(6), 737-750.

Wei, T., Peakall, J., Parsons, D. R., Chen, Z., Zhao, B. & Best, J. (2013) Three-dimensional gravity-current flow within a subaqueous bend: Spatial evolution and force balance variations. *Sedimentology*, 60(7), 1668-1680.

Weidner, R. T. S., Robert L; Walters, Arthur E (1975) *Elementary Physics, Classical and Modern*. Boston: Allyn & Bacon.

Wells, M. G. & Dorrell, R. M. (2021) Turbulence Processes Within Turbidity Currents. *Annual Review of Fluid Mechanics*, 53(1), 59-83.

White, F. M. (1999) *Fluid mechanics*. Boston: WCB McGraw- Hill, Inc.